CARDIFF UNIVERSITY
PRIFYSGOL CAERDYDD

ORCA – Online Research @ Cardiff

This is an Open Access document downloaded from ORCA, Cardiff University's institutional repository:https://orca.cardiff.ac.uk/id/eprint/145285/

This is the author's version of a work that was submitted to / accepted for publication.

Citation for final published version:

Zhang, Xu, Barker, Stephen , Knorr, Gregor, Lohmann, Gerrit, Drysdale, Russell, Sun, Youbin, Hodell, David and Chen, Fahu 2021. Direct astronomical influence on abrupt climate variability. Nature Geoscience 14 , 819–826. 10.1038/s41561-021-00846-6

Publishers page: http://dx.doi.org/10.1038/s41561-021-00846-6

Please note:
Changes made as a result of publishing processes such as copy-editing, formatting and page numbers may not be reflected in this version. For the definitive version of this publication, please refer to the published source. You are advised to consult the publisher's version if you wish to cite this paper.

This version is being made available in accordance with publisher policies. See http://orca.cf.ac.uk/policies.html for usage policies. Copyright and moral rights for publications made available in ORCA are retained by the copyright holders.

Direct astronomical influence on abrupt climate variability

Xu Zhang[1,2*], Stephen Barker[3], Gregor Knorr[4], Gerrit Lohmann[4], Russell Drysdale[5], Youbin Sun[6], David Hodell[6], Fahu Chen[1,2]

[1] Group of Alpine Paleoecology and Human Adaptation (ALPHA), State Key Laboratory of Tibetan Plateau Earth System, Resources and Environment (TPESRE), Institute of Tibetan Plateau Research, Chinese Academy of Sciences, Beijing 100101, China
[2] Key Laboratory of Western China's Environmental Systems (Ministry of Education), College of Earth and Environmental Science, Lanzhou University, Lanzhou 730000, China
[3] School of Earth and Ocean Sciences, Cardiff University, Cardiff CF10 3AT, UK
[4] Alfred Wegener Institute Helmholtz Center for Polar and Marine Research, 27570 Bremerhaven, Germany
[5] School of Geography, Earth and Atmospheric Sciences, The University of Melbourne, Parkville 3010, Victoria, Australia
[6] State Key Laboratory of Loess and Quaternary Geology, CAS Center for Excellence in Quaternary Geology and Global changes, Institute of Earth Environment, Chinese Academy of Sciences, Xiaan 710061, China
[7] Godwin Laboratory for Paleoclimate Research, Department of Earth Sciences, University of Cambridge, Cambridge, UK

*Correspondence to: xu.zhang@itpcas.ac.cn

ORCID iD: 0000-0003-1833-9689

Abstract

Changes in the magnitude of millennial-scale climate variability (MCV) during the Late Pleistocene occur as a function of changing background climate state over tens of thousands of years, an indirect consequence of slowly-varying incoming solar radiation associated with changes in Earth's orbit. However, whether astronomical forcing can stimulate MCV directly (without a change in background state) remains elusive. Here, we use a comprehensive fully-coupled climate model to demonstrate that orbitally-driven insolation changes alone can give rise to spontaneous millennial-scale climate oscillations under intermediate glacial conditions. Our results demonstrate

that an abrupt transition from warm interstadial to cold stadial conditions can be triggered directly by a precession-controlled increase in low-latitude boreal summer insolation and/or an obliquity-controlled decrease in high-latitude mean annual insolation, by modulating North Atlantic low-latitude hydroclimate and/or high-latitude sea ice-ocean-atmosphere interactions respectively. Furthermore, contrasting insolation effects over the tropical versus subpolar North Atlantic, exerted by obliquity or precession, result in an oscillatory climate regime even within an otherwise stable climate. With additional sensitivity experiments under different glacial-interglacial climate backgrounds, we further synthesize a coherent theoretical framework for climate stability, elaborating the direct/indirect (dual) controls of Earth's orbital cycles on millennial-scale climate variability during the Pleistocene.

Main Text:

Glacial-interglacial (G-IG) cycles are the primary feature of Earth's climate during the Pleistocene and occur at periodicities that are linked to changes in Earth's orbit[1,2]. Co-evolving with G-IG cycles is millennial-scale climate variability (MCV)[3–7], also known as Dansgaard-Oeschger (DO) cycles in Greenland ice cores during the last glacial period[8]. These large and repeated millennial-scale oscillations between stadial and interstadial conditions have been associated with changes in the mode of Atlantic Meridional Overturning Circulation (AMOC)[9–13]. Since its occurrence extends back to at least 800 thousand years before present (ka BP) in the ice core record[14], MCV has been acknowledged as a ubiquitous feature of glacial climate[5,7,14]. Earth's orbit, as the fundamental external driver of the climate system[1], has also left its imprints in MCV – e.g. the magnitude of the MCV contains evident periodicities of Earth's precession, obliquity and eccentricity[15–18] (Fig. 1a-c). This relationship has been proposed to be related to the dependence

of MCV on G-IG changes in climate background state (i.e. ice volume and greenhouse gas concentrations) (Fig. 1d)[4] , which is also supported by the robust coherent ~100-kyr periodicity between millennial activity and Earth's orbit (Fig. 1c). The associated dynamics have been widely investigated by fully coupled climate models and synthesized by a conceptual framework of AMOC nonlinearity/bi-stability[9,10,12,19]. We refer to this as the *indirect* role of orbital changes on MCV. Meanwhile, the clear coherent periodicity of ~21- and 40-kyr (Fig. 1c.) motivates us to ask if changes in orbital configuration might give rise to MCV directly, e.g. by modulating the strength and/or mode of the AMOC, especially during intermediate glacial periods when climate boundary conditions are relatively stable in comparison to transitions between glacial and interglacial states (that is, the *direct* role). The potential importance of this role has been tentatively explored by conceptual and simple dynamical system models[20,21]. However, results are inconclusive due to lack of support from fully coupled climate models that include more advanced climate physics.

Using an atmosphere-ocean fully coupled climate model, we aim to assess whether insolation changes alone can give rise to changes in the state of the AMOC that resemble DO events. Because different internal climate components (e.g. atmospheric CO_2, ice volume, ocean circulation, etc.) are tightly interconnected[22–24], it is important to identify an appropriate time interval in which the occurrences of MCV can be attributed to insolation changes alone. Based on available proxy records[25,26], we have selected a period during the latter stage of Marine Isotope Stage (MIS) 3 (40–32 ka BP), during which DO events 5 to 7 occurred in succession and apparently were not greatly influenced by changes in ice volume and atmospheric CO_2. Note that we do not aim to reproduce these recorded DOs by varying full boundary conditions during this period but rather to employ them as a surrogate for a systematic and generic understanding of AMOC responses to changes in Earth's orbit under intermediate glacial conditions. With the aid of transient and equilibrium

experiments, we confirm that orbital changes alone can directly account for the occurrences of MCV.

Spontaneous AMOC oscillation

We first conducted a transient experiment (TRN40ka) with gradual changes in orbital settings from 40 ka to 32 ka BP[27], based on an equilibrium baseline experiment (E40ka_CTL) in which the full boundary conditions of 40 ka BP are imposed for 5000 years (Methods, Extended Data Fig. 1 and Extended Data Table 1). Following a mono-stable strong AMOC mode before 37 ka BP, the AMOC starts to fluctuate abruptly into and out of a weak AMOC phase in TRN40ka with a periodicity of ~1200 years (Fig. 2a-c, Extended Data Fig. 2a-e), notably resembling DOs 5-7[28]. The simulated climate changes from weak to strong AMOC phases – e.g. warming/cooling in the North/South Atlantic, northward shift of the Intertropical Convergence Zone (ITCZ) – are also in general agreement with the observed features of DOs during the MIS3 (Extended Data Fig. 3a, b and Extended Data Table 2, 3). Therefore, the orbitally-induced AMOC changes in our model provide a reasonable representation of MCV under intermediate glacial conditions.

To further test whether MCV might be a result of an unforced AMOC oscillation under constant orbital settings, we performed an equilibrium experiment (E40ka_34kaOrb) spanning ~5500 years by changing orbital parameters of E40ka_CTL from 40 ka BP to 34 ka BP. Although the orbital change applied is instantaneous (unlike the actual sinusoidal change), the long-term constant forcing enables us to unequivocally evaluate equilibrated climate responses and hence AMOC stability characteristics with respect to orbital change, a principle adopted in previous studies[10,12,19]. Note that 34 ka BP is a period corresponding to the successive DOs 5-7, during which the internal climate background (i.e. ice volume[26] and atmospheric CO_2 level[25]) are relatively constant and similar to those during 40 ka BP. This lends credibility to the idea that these DOs might be a result

of the existence of an AMOC oscillatory state. It appears that the AMOC shifts from a mono-stable strong mode in E40ka_CTL (Extended Data Fig. 1) to a stable oscillatory mode in E40ka_34kaOrb (Fig. 2d and Extended Data Fig. 2f-j). Characteristics of simulated AMOC oscillatory changes and associated global climate responses are similar to those in TRN40ka (Fig. 2c, d and Extended Data Fig. 3c, d), which is also consistent with reconstructed features of DOs. These confirm the existence of a supercritical Hopf Bifucation[29] associated with an orbitally-controlled stable regime that has poised the AMOC for self-oscillation, accounting for the occurrences of MCV.

Governing dynamics

Earth's orbit consists of three parameters (i.e. eccentricity, precession and obliquity), which exert different effects on the tempo-spatial distribution of insolation across the Earth[27]. To identify their individual roles on AMOC stability, we performed two further equilibrium runs in which either eccentricity-modulated precession or obliquity at 34 ka BP is imposed in E40ka_CTL (Fig. 3, Extended Data Fig. 4). Both experiments are characterized by unforced AMOC oscillations, indicating that either an enhanced boreal seasonality due to a decrease in precession (E40ka_34kaEP) or an increased latitudinal insolation gradient associated with a lowered obliquity (E40ka_34kaObl) can generate a glacial climate background state under which the AMOC oscillates spontaneously.

In the scenario with enhanced boreal seasonality (E40ka_34kaEP), warmer boreal summers prompt sea-ice reduction and hence increases the open-water area in the subpolar NA (Extended Data Fig. 5d, e, g, h), which has the potential to enhance ocean heat loss during the colder boreal winter. This tends to strengthen North Atlantic Deep Water (NADW) formation by thermally increasing surface water mass density and hence reducing the vertical density stratification. However, mean annual net precipitation increases synchronously over the tropical NA, effectively

reducing sea-surface salinity (Fig. 3c, and Extended Data Fig. 5f, i). The intensity of the western Atlantic summer warm pool has been proposed to play an important role on Atlantic-to-Pacific atmospheric moisture export by modulating trade-wind strength, and hence the net precipitation and sea-surface salinity in the subtropical NA[30]. In E40ka_34kaEP, the enhanced boreal summer insolation strengthens the warm pool intensity, leading to a basin-wide low-pressure anomaly[31] and hence a weakened atmospheric moisture export[30] (Fig. 3c). This chain of processes is further confirmed by our sensitivity experiments in an atmospheric general circulation model – i.e. tropical NA warming alone can reproduce the similar climate response as illustrated in Fig. 3c (Extended Data Fig. 7). Thereafter, northward transport of these freshened tropical water masses tends to decrease surface water density in the key convection sites of the NA, enhancing the vertical density stratification and eventually reducing NADW formation. As an equilibrated response to the increased summer insolation, the tropical freshening effect finally surpasses the subpolar warming effect, leading to AMOC transition into its weak phase (Fig. 3a-c and Extended Data Fig. 4a-e).

In E40ka_34kaObl, the lowered obliquity causes mean warming over the low latitudes but cooling over the high latitudes (i.e. the scenario with enhanced latitudinal insolation gradient). The former increases sea-surface salinity in the tropical NA by enhancing the atmospheric moisture export from the western tropical NA to the eastern equatorial Pacific, owing to differential heating responses between them[12] (Extended Data Fig. 5a, c). This tropical hydro-climate response tends to promote the formation of NADW by supplying saltier tropical water masses to the convection sites. However, high-latitude cooling at times of low obliquity decreases sea-surface temperature and expands sea-ice cover in the subpolar NA, reducing the open-water area where deep convection occurs and hence decreases AMOC strength simultaneously (Extended Data Fig. 5b). Under intermediate glacial conditions, sea-ice cover in the subpolar NA is close to a threshold

which governs the switch between its interstadial and stadial states[10] (Extended Data Fig. 1b-e). As an equilibrated response to the lowered obliquity, the high-latitude cooling effect finally surpasses the low-latitude salinification effect, thereby leading to AMOC reduction (Fig. 3d-f).

Once a transition into the weak AMOC phase is stimulated by orbital changes (i.e. TRN40ka), the contemporary constant orbital settings allow the continuation of unforced AMOC self-oscillations (i.e. E40ka_34kaOrb). As the AMOC is in its weak phase, gradual subsurface warming of the subpolar ocean and increasing northward salinity transport in the NA work together to return AMOC to its strong phase. A gradual cooling in the NA convection sites and decrease in the northward transport of saltwater cause AMOC weakening, up to a point at which the AMOC reduces abruptly and the weak phase returns (Extended Data Fig. 2 and 4). Furthermore, abrupt transitions into and out of the weak phases can be attributed to the atmosphere-ocean-sea ice positive feedback in the NA convection sites[10,32]. Therefore, the unforced AMOC self-oscillation is a consequence of internal climate feedbacks between the low-latitude hydro-climate and the high-latitude atmosphere-ocean-sea ice system, similar to mechanisms described for "thermohaline oscillations"[33–35]. Beyond this, our results elaborate that changes in orbital parameters can modulate the NA thermohaline balance by exerting contrasting effects on NADW formation over the low versus high latitudes, generating an intrinsically oscillatory state accounting for MCV under intermediate glacial conditions.

Roles of internal climate backgrounds

Previous studies have suggested that the interplay between changes in atmospheric CO_2 and ice volume can control the sensitivity of AMOC to applied perturbations[9,10,12,19], giving rise to intermediate glacial conditions that are characterized by high MCV activity (i.e. the *indirect* control of Earth's orbit on MCV) (Fig. 1d). Indeed, no AMOC mode changes are induced in our

experiments under peak glacial and interglacial conditions even under the most extreme changes in orbital configurations (Extended Data Fig. 7, Methods). This corroborates the dominant roles of ice volume under glacial maximum conditions and of atmospheric CO_2 during peak interglacial periods on AMOC stability during these times[10,12]. In contrast, during intermediate glacial periods, millennial-scale variations in atmospheric CO_2 of ~20 ppm[36,37] and ice volume of ~18 meters equivalent sea level (m.e.s.l.)[38] are potentially enough to alter the sensitivity of the AMOC to orbital changes. To test this hypothesis, we have performed two sets of equilibrium sensitivity experiments incorporating changes in either atmospheric CO_2 (Fig. 4) or ice volume (Fig. 5) based on experiment E40ka_34kaOrb that is characterized by an oscillatory AMOC state (Extended Data Table 1, Methods).

In the two CO_2 sensitivity experiments in which atmospheric CO_2 level is either increased or decreased by 10 ppm, spontaneous AMOC oscillations are maintained (Fig. 4). Importantly, it appears that decreasing atmospheric CO_2 is capable of reducing interstadial duration, thereby shortening the oscillation period (Fig. 4e, f), a concept which is consistent with ice-core records[7] (Methods). Given that AMOC changes and associated global responses can alter atmospheric CO_2 levels[22,39], this suggests that millennial-scale CO_2 changes can serve as an internal climate agent accounting for observed changes in timing characteristics of MCV during glacial periods.

In contrast, the AMOC is shifted to a stable weak mode in the ice-sheet sensitivity experiment in which Northern Hemisphere ice sheets are replaced by those at 50 ka BP, which corresponds to ~12 m.e.s.l. lower than those at 40 ka BP (Phase A in Fig. 5). Further increasing obliquity and precession (directionally opposite to the orbital changes from 40 to 34 ka BP) can cause a return to a stable oscillatory mode of AMOC (i.e. Phase A to B in Fig. 5), in which oscillating characteristics are further determined by the magnitudes of these orbital changes (i.e. Phase B

versus C in Fig. 5; Methods). These results suggest that lowering Northern Hemisphere ice sheets can lead to a shift of the oscillatory regime towards higher values of obliquity and precession, due to changes in wind stress promoting sea-ice expansion and cooling across the northern NA[10].

Overall, these results suggest that climate backgrounds associated with Northern Hemisphere ice-sheet configuration and atmospheric CO_2 level determine the sensitivity of the AMOC to orbitally-induced insolation changes and hence the window of the AMOC oscillatory regime in the phase space of Earth's orbital cycles (Fig. 6). Accordingly, although MCV contains evident obliquity and precessional periodicities[15–18], its amplitude does not always follow the magnitude of associated insolation changes[40].

Oscillatory climate regime in glacial cycle

In contrast to previous studies[20,21], the model used here, with more advanced climate physics, enables us to elaborate on the comprehensive dynamics of the AMOC oscillatory regime associated with changes in Earth's orbit (i.e. precession and obliquity) during intermediate glacial periods (i.e. the *direct* control of Earth's orbit on MCV and abrupt climate shifts). As a result of changes in either eccentricity-modulated precession or obliquity, climate variations over the tropical and subpolar NA exert contrasting effects on the strength of the AMOC, thereby resulting in a climate background state under which unforced AMOC oscillations can occur. In particular, the subpolar thermal effect (associated with obliquity-controlled mean annual insolation) and the tropical salt effect (associated with precession-controlled summer insolation) represent the crucial triggering mechanisms of AMOC changes in response to slow variations in Earth's orbit.

Based on the simulations in this study, we therefore synthesize a conceptual framework to describe the stable AMOC oscillatory regime in the phase space of Earth's obliquity and eccentricity-modulated precession under different internal climate backgrounds spanning G-IG cycles (Fig. 6)

– i.e. a framework representing the dual controls of astronomical forcing on MCV. In particular, this indicates that the oscillatory regime is a function not only of Earth's orbit under intermediate glacial conditions (Fig. 2, 3), but also of global ice volume and (probably) atmospheric CO_2 (Fig. 5 and Extended Data Fig. 7). Note that this regime exists only under intermediate glacial conditions given the overriding influence of glacial maximum ice sheets and peak interglacial CO_2 on AMOC (mono)stability[10,12]. A recent model study[41] proposed that, under peak interglacial conditions, insolation changes alone can trigger abrupt AMOC weakening. However, the typical magnitude of AMOC weakening in their study (~5Sv) is significantly less than AMOC changes reported here (~20Sv). Additionally, the cooling events in their proxy records are of variable intensity and the relatively strong cooling events (e.g. associated with MIS17c[41]) appear to consistently occur under intermediate glacial conditions as defined by benthic $\delta^{18}O$ and atmospheric CO_2 in this study (Fig. 1d). Their findings[41] therefore support our contention that background climate plays a key role in the magnitude of MCV.

A significant advantage of this framework to explain the occurrences of MCV is the independence from additional perturbations (e.g. freshwater input), whose origins are too uncertain to pin down as triggers of AMOC changes[42,43] (on the contrary, changes in Earth's orbit can be unequivocally calculated[27,44]). Therefore, our framework can account for a broader spectrum of MCV in global climate archives. For example, during MIS3 some DO events (e.g. DOs 5-7) that occurred without evident changes in atmospheric CO_2[25] and ice volume[26] can be explained by the orbitally-induced AMOC oscillatory regime. Furthermore, given the small ratio of the number of Heinrich Events (HEs, massive iceberg releasing events) to DO cycles during MIS3[45] and the triggering dynamics of HEs[23,46], our framework implies that HEs might be considered as a particular case of orbitally-

induced MCV when Laurentide marine-based ice shelves become susceptible to subsurface warming in a weak AMOC phase.

In addition, our framework suggests that abrupt climate change could be attributed to the *direct* role of orbital change when contemporary changes in ice volume and atmospheric CO_2 exert opposite effects on the strength of the AMOC[10,12].

Overall, our framework represents the dual controls of changes in Earth's orbit (i.e. the *direct* and *indirect* controls) on climate variability at millennial time scales. The former – our finding in this study – complements the classic Milankovitch theory[44] used to explain the latter, providing a coherent theoretical framework for understanding the origins of MCV and its activity across time. In particular, over the last 800kyr, astronomical forcing can directly account for occurrences of MCV when the climate background, driven by Milankovitch cycles, is in an intermediate state as defined by benthic $\delta^{18}O$ and atmospheric CO_2 (Fig. 1d). Our results imply that MCV may also have been a direct consequence of astronomical forcing during the Early and Mid-Pleistocene when glacial cycles were characterized by different intensities and periodicities from those during the Late Pleistocene[47,48]. This is highlighted by a new 1500 kyr-long MCV stack that consists of four centennial-scale proxies from mid-latitude Northern Hemisphere[49]. In the real world, internal climate components (e.g. ice volume, atmospheric CO_2, ocean currents, etc.) are closely coupled[22–24] when responding to orbital changes[1]. To assess this improved Milankovitch theory in the future, Earth System models with interactive ice-sheet and carbon-cycle feedbacks are therefore required to explore the full dynamics associated with co-evolution of millennial- and orbital-scale climate variability during the Pleistocene.

Acknowledgments:

We thank colleagues at the Alfred Wegener Institute Helmholtz Centre for Polar and Marine Research in Bremerhaven for maintaining the supercomputer. The study is supported by Basic Science Center for Tibetan Plateau Earth System (BSCTPES, NSFC project No. 41988101), Natural Science Foundation of China (No. 42075047) and German Helmholtz Postdoc Program (PD-301). We also acknowledge financial support from UK NERC (grants NE/J008133/1 and NE/L006405/1) to S.B. and German BMBF funded project PalMod (01LP1504A, 01LP1915A and 01LP1916B) and PACES program of the AWI to G.K and G.L. A sabbatical visit by R.D. to AWI was financially supported by the Faculty of Science at the University of Melbourne.

Author Contributions:

X.Z. conceived and developed the research, and wrote the manuscript with the help of S.B. and G.K. All authors contributed to the final version of the manuscript.

Competing interests:

The authors declare no competing financial interests.

Figure Legends

Figure 1. Relationship of millennial-scale climate activity with Earth's orbit and glacial-interglacial cycles in the last 800 ka. **a.** 0.5-5 kyr Taner filter (blue) of %NPS (*Neogloboquadrina pachyderma sinistral*) in the northern North Atlantic[50] with its amplitude calculated by Hilbert transform (red) (Methods). **b.** Eccentricity-tilt-precession (ETP) index[27]. **c.** Wavelet coherence analysis between the millennial-scale activity (red curve in a) and ETP index (Methods). **d.** Millennial-scale activity in the glacial-interglacial phase space with respect to atmospheric CO_2[37] and the benthic $\delta^{18}O$ stack[2] over the last 800 ka (cf. red curve in panel a). Color represents mean

amplitude of the millennial-scale activity in a 0.05 per mil (benthic $\delta^{18}O$ value) and 2 ppm (atmospheric CO_2 value) grid. Grids that include only one data point are ignored. It appears that periods of high millennial-scale activities mainly occurred under intermediate glacial conditions (i.e. rectangle in panel d). All records are anchored to the AICC2012 age model and evenly re-interpolated to 0.2-kyr resolution for the analysis (Methods).

Figure 2. Orbitally-induced AMOC oscillatory regime. a, b, Imposed changes in obliquity and precession and **c,** simulated AMOC index in experiment TRN40ka**.** Note that the initial part (40-37.5 ka BP) of TRN40ka is accelerated by a factor of 10 (i.e. 2500 calendar years are represented by 250 model years) (Methods). **d.** AMOC index in experiment E40ka_34kaOrb, representing the AMOC response to constant orbital settings of 34 ka BP under intermediate glacial conditions.

Figure 3. Triggering dynamics of orbitally induced AMOC changes. a, b Imposed precession changes and simulated AMOC index in experiment E40ka_34kaEP (i.e. only changing eccentricity-modulated precession in E40ka_CTL); **d, e** applied obliquity changes and simulated AMOC index in experiment E40ka_34kaObl (i.e. only changing obliquity in E40ka_CTL). **c, f** Anomalies between the mean climatology before the onset of abrupt AMOC reduction in E40ka_34kaEP (c) and E40ka_34kaObl (d) and the mean climatology of control run E40ka_CTL, representing climate tendency after changes in precession and obliquity, respectively. The climatology in E40ka_34kaEP and E40ka_34kaObl is represented by 40- and 100-year-average of the period indicated by the red and blue bold line in (b) and (e), respectively. In **c)**, shaded for total net freshwater flux (units: mm/day), vector for vertical integrated moisture transport (units: kg m^{-1} s^{-1}) and contour for sea-level pressure (units: Pa). In **f)**, shaded for sea-ice concentration (units: %), and contour for vertical mixed layer depth (units: m).

Figure 4. Responses of AMOC oscillatory regime to millennial-scale CO_2 changes. a, b Imposed CO_2 changes; **c, d** simulated AMOC indices; and **e, f** wavelet analysis of corresponding AMOC index in the decreasing and increasing CO_2 experiment. Both CO_2 sensitivity runs are initialized from the 2050th model year of E40ka_34kaOrb, as indicated by the vertical dash lines. Therefore, the 2051st-7500th model years to the righthand side of the dash line correspond to the CO_2 equilibrium runs, while to the left is for E40ka_34kaOrb. As the CO_2 level is decreased (increased) by 10 ppm, the dominant periodicity of AMOC oscillations (~1200 years) is shortened (prolonged) to ~1000 (~1500) years after 5000 model years, as shown in panel e (f).

Figure 5. Response of the AMOC oscillatory regime to varying intermediate glacial conditions. a, b, c, d Imposed changes in northern hemisphere ice sheets (a), atmospheric CO_2 level (b), precession parameter (c) and obliquity (d). **e,** Simulated AMOC index derived in turn from E40ka_34kaOrb, E40ka_34kaOrb_50kaICE (Phase A), E40ka_50kaICE (Phase B) and E50ka (Phase C), which represent stepwise changes in boundary conditions. Note that each experiment is initialized from the quasi-equilibrium ocean state of the previous experiment, consistent with the principle to investigate AMOC hysteresis/stability behavior (Extended Data Table 1).

Figure 6. Conceptual framework for AMOC oscillatory regime in the phase space of Earth's orbit under different climate backgrounds. **a**, Obliquity- and **b**, eccentricity-modulated precession controlled AMOC oscillatory regime under different climate backgrounds that are represented by the color scheme. Upper x-axis in each panel represents the governing dynamics of changes in the strength of the AMOC, associated with changes in the corresponding orbital parameters as shown in the lower x-axis. Climate background conditions are controlled by changes in ice volume and atmospheric greenhouse gases[10,12]. Stars are indicative of orbital sensitivity runs

under peak glacial (blue) and interglacial conditions (red) when orbital changes alone cannot directly give rise to AMOC mode transitions (Extended Data Fig. 7). The green and light blue lines represent scenarios under intermediate glacial conditions with relatively warm and cold NA, respectively (in this case, the difference between warm and cold NA conditions reflects changes in ice-sheet size but we hypothesize that CO_2 has an equivalent effect for changes in CO_2 larger than we impose in this study). That is, the warm (cold) NA conditions correspond to scenarios with high (low) intermediate ice sheets that lead to a low (high) sensitivity of the AMOC to forcing changes[10].

References:

1. Hays, J. D., Imbrie, J. & Shackleton, N. J. J. . Variations in the Earth ’ s Orbit : Pacemaker of the Ice Ages. *Science (80-.).* **194**, 1121–1132 (1976).

2. Lisiecki, L. E. & Raymo, M. E. A Pliocene-Pleistocene stack of 57 globally distributed benthic δ 18 O records. *Paleoceanography* **20**, 1–17 (2005).

3. Raymo, M. E., Ganley, K., Carter, S., Oppo, D. W. & McManus, J. Millennial-scale climate instability during the early Pleistocene epoch. *Nature* **392**, 699–702 (1998).

4. McManus, J. F., Oppo, D. W. & Cullen, J. L. A 0.5-Million-Year Record of Millennial-Scale Climate Variability in the North Atlantic. *Science (80-.).* **283**, 971–975 (1999).

5. Jouzel, J. *et al.* Orbital and millennial antarctic climate variability over the past 800,000 years. *Science (80-.).* **317**, 793–796 (2007).

6. Hodell, D. A. & Channell, J. E. T. Mode transitions in Northern Hemisphere Glaciation: Co-evolution of millennial and orbital variability in Quaternary climate. *Clim. Past* **12**, 1805–1828 (2016).

7. Brook, E. J. & Buizert, C. Antarctic and global climate history viewed from ice cores. *Nature* **558**, 200–208 (2018).

8. Dansgaard, W. *et al.* Evidence for general instability of past climate from a 250-kyr ice-core record. *Nature* **364**, 218–220 (1993).

9. Ganopolski, A. & Rahmstorf, S. Rapid changes of glacial climate simulated in a coupled climate model. *Nature* **409**, 153–158 (2001).

10. Zhang, X., Lohmann, G., Knorr, G. & Purcell, C. Abrupt glacial climate shifts controlled by ice sheet changes. *Nature* **512**, 290–294 (2014).

11. Peltier, W. R. & Vettoretti, G. Dansgaard-Oeschger oscillations predicted in a comprehensive model of glacial climate: A 'kicked' salt oscillator in the Atlantic. *Geophys. Res. Lett.* **41**, 7306–7313 (2014).

12. Zhang, X., Knorr, G., Lohmann, G. & Barker, S. Abrupt North Atlantic circulation changes in response to gradual CO 2 forcing in a glacial climate state. *Nat. Geosci.* **10**, 518–523 (2017).

13. Lynch-Stieglitz, J. The Atlantic Meridional Overturning Circulation and Abrupt Climate Change. *Ann. Rev. Mar. Sci.* **9**, 83–104 (2017).

14. Barker, S. *et al.* 800,000 Years of Abrupt Climate Variability. *Science (80-.).* **334**, 347–351 (2011).

15. Siddall, M., Rohling, E. J., Blunier, T. & Spahni, R. Patterns of millennial variability over the last 500 ka. *Clim. Past* **6**, 295–303 (2010).

16. Cheng, H. *et al.* The Asian monsoon over the past 640,000 years and ice age terminations. *Nature* **534**, 640–646 (2016).

17. McIntyre, A. & Molfinot, B. Forcing of Atlantic Equatorial and Subpolar Millennial Cycles by Precession. *Science (80-.).* **274**, 1867–1870 (1996).

18. Thirumalai, K., Clemens, S. C. & Partin, J. W. Methane, Monsoons, and Modulation of Millennial-Scale Climate. *Geophys. Res. Lett.* **47**, (2020).

19. Zhang, X., Prange, M., Merkel, U. & Schulz, M. Instability of the Atlantic overturning circulation during Marine Isotope Stage 3. *Geophys. Res. Lett.* **41**, 4285–4293 (2014).

20. Rial, J. A. & Yang, M. Is the frequency of abrupt climate change modulated by the orbital insolation? *Geophys. Monogr. Ser.* **173**, 167–174 (2007).

21. Mitsui, T. & Crucifix, M. Influence of external forcings on abrupt millennial - scale climate changes : a statistical modelling study. *Clim. Dyn.* **48**, 2729–2749 (2017).

22. Schmittner, A. & Galbraith, E. D. Glacial greenhouse-gas fluctuations controlled by ocean circulation changes. *Nature* **456**, 373–376 (2008).

23. Marcott, S. A. *et al.* Ice-shelf collapse from subsurface warming as a trigger for Heinrich events. *Proc. Natl. Acad. Sci. U. S. A.* **108**, 13415–9 (2011).

24. Markle, B. R. *et al.* Global atmospheric teleconnections during Dansgaard-Oeschger events. *Nat. Geosci.* **10**, 36–40 (2017).

25. Ahn, J. & Brook, E. J. Siple Dome ice reveals two modes of millennial CO2 change during the last ice age. *Nat. Commun.* **5**, 3723 (2014).

26. Grant, K. M. *et al.* Rapid coupling between ice volume and polar temperature over the past 150,000 years. *Nature* **491**, 744–747 (2012).

27. Berger, A. Long-Term Variations of Caloric Insolation from the Earth's Orbital Elements. *Quat. Res.* **9**, 139–167 (1978).

28. Grootes, P. M. & Stuiver, M. Oxygen 18/16 variability in Greenland snow and ice with 10-3 to 105-year time resolution. *J. Geophys. Res. Ocean.* **102**, 26455–26470 (1997).

29. Marsden, J. E., McCracken, M., Sethna, P. R. & Sell, G. R. The Hopf Bifurcation and Its Applications. *J. Appl. Mech.* (1978) doi:10.1115/1.3424264.

30. Wang, C., Zhang, L. & Lee, S.-K. Response of Freshwater Flux and Sea Surface Salinity to Variability of the Atlantic Warm Pool. *J. Clim.* **26**, 1249–1267 (2013).

31. Gill, A. E. Some simple solutions for heat-induced tropical circulation. *Q. J. R. Meteorol. Soc.* **106**, 447–462 (1980).

32. Li, C. & Born, A. Coupled atmosphere-ice-ocean dynamics in Dansgaard-Oeschger events. *Quaternary Science Reviews* vol. 203 1–20 (2019).

33. Winton, M. Deep Decoupling Oscillations of the Oceanic Thermohaline Circulation. in *Ice in the Climate System* (ed. Peltier, W. R.) 417–432 (Springer Berlin Heidelberg, 1993).

34. Brown, N. & Galbraith, E. D. Hosed vs. unhosed: Interruptions of the Atlantic Meridional Overturning Circulation in a global coupled model, with and without freshwater forcing. *Clim. Past* **12**, 1663–1679 (2016).

35. Broecker, W. S., Bond, G., Klas, M., Bonani, G. & Wolfli, W. A Salt Oscillator in the Glacial Atlantic? 1. The Concept. *Paleoceanography* **5**, 469–477 (1990).

36. Ahn, J. & Brook, E. J. Atmospheric CO2 and climate on millennial time scales during the last glacial period. *Science (80-.).* **83**, 83–85 (2008).

37. Bereiter, B. *et al.* Revision of the EPICA Dome C CO2 record from 800 to 600 kyr before present. *Geophys. Res. Lett.* **42**, 1–8 (2015).

38. Siddall, M., Rohling, E. J., Thompson, W. G. & Waelbroeck, C. Marine Isotope Stage 3 Sea Level Fluctuations: Data Synthesis and New Outlook. *Rev. Geophys.* **46**, RG000226 (2008).

39. Gottschalk, J. *et al.* Mechanisms of millennial-scale atmospheric CO_2 change in numerical model simulations. *Quat. Sci. Rev.* **220**, 30–74 (2019).

40. Billups, K. & Scheinwald, A. Origin of millennial-scale climate signals in the subtropical North Atlantic. *Paleoceanography* **29**, 612–627 (2014).

41. Yin, Q. Z., Wu, Z. P., Berger, A., Goosse, H. & Hodell, D. Insolation triggered abrupt weakening of Atlantic circulation at the end of interglacials. *Science* **373**, 1035–1040 (2021).

42. Dokken, T. M., Nisancioglu, K. H., Li, C., Battisti, D. S. & Kissel, C. Dansgaard-Oeschger cycles: interactions between ocean and sea ice intrinsic to the Nordic Seas. *Paleoceanography* **28**, 491–502 (2013).

43. Barker, S. *et al.* Icebergs not the trigger for North Atlantic cold events. *Nature* **520**, 333–336 (2015).

44. Milanković, M. *Kanon der Erdbestrahlung und seine Anwendung auf das Eiszeitenproblem*. *Royal Serbien Sciences, Special Publications 132, Section of Mathematical and Natural Sciences* vol. 133 (1941).

45. Heinrich, H. Origin and consequences of cyclic ice rafting in the Northeast Atlantic Ocean during the past 130,000 years. *Quat. Res.* **29**, 142–152 (1988).

46. Bassis, J. N., Petersen, S. V. & Mac Cathles, L. Heinrich events triggered by ocean forcing and modulated by isostatic adjustment. *Nature* **542**, 332–334 (2017).

47. Shackleton, N. J. & Opdyke, N. D. Oxygen-isotope and paleomagnetic stratigraphy of pacific core V28-239 late Pliocene to latest Pleistocene. *Mem. Geol. Soc. Am.* **145**, (1976).

48. Pisias, N. G. & Moore, T. C. The evolution of Pleistocene climate: A time series approach. *Earth Planet. Sci. Lett.* **52**, (1981).

49. Sun, Y. *et al.* Persistent orbital influence on millennial climate variability through the Pleistocene. *Nat. Geosci.* 1–7 (2021) doi:10.1038/s41561-021-00794-1.

50. Barker, S. *et al.* Early Interglacial Legacy of Deglacial Climate Instability. *Paleoceanogr. Paleoclimatology* **34**, 1455–1475 (2019).

Methods

Timeseries analysis

Bandpass filtering was performed on evenly resampled (0.2kyr) timeseries using a Taner filter (roll-off rate = 10^12) by Matlab function presented by Linda A. Hinnov (http://mason.gmu.edu/~lhinnov/cyclostratigraphytools.html). Hilbert transforms of the bandpass filtered series were also implemented using Linda A. Hinov's Matlab function. Wavelet analyses were produced using the Matlab function presented by Grinsted et al.[51], implemented on evenly resampled (0.2kyr) timeseries.

Model description

We use a comprehensive fully coupled atmosphere–ocean general circulation model (AOGCM), COSMOS (ECHAM5-JSBACH-MPI-OM) in this study. The atmospheric model ECHAM5[52], complemented by the land surface component JSBACH[53], is used at T31 resolution (~3.75°), with 19 vertical layers. The ocean model MPI-OM[54], including sea-ice dynamics that is formulated using viscous-plastic rheology[55], has a resolution of GR30 (3°×1.8°) in the horizontal, with 40 uneven vertical layers. The climate model has already been used to investigate a range of paleoclimate phenomena[56–60], especially millennial-scale abrupt glacial climate changes[10,12]. This indicates that it is capable of capturing the nonlinear behavior of the glacial climate system and is thus a very suitable climate model for this study.

Experimental details

All experiments done in this study are listed in Extended Data Table 1. A detailed introduction of each kind of experiments and their rationality are present as follows.

1. MIS3 baseline experiment

We first conduct an equilibrated control simulation (E40ka_CTL) by imposing the fixed boundary conditions of 40ka BP. Specifically, during 40ka BP the three orbital parameters, i.e. eccentricity,

precession of the equinoxes (the angle between the Earth's position during the Northern Hemisphere vernal equinox and the orbit perihelion), and obliquity, are 0.013146, 358.17°, and 23.61°, respectively[27]; the greenhouse gases CO_2, CH_4 and N_2O, are 195 ppm, 413 ppb and 231 ppb, respectively[25,61]. The ice-sheet configuration is a combination of ice-sheet reconstructions from ICE-5G[62] and Paleoclimate Model Inter-comparison Project 3 (PMIP3). That is, we first calculated the topography anomaly between 40ka BP and the Last Glacial Maximum (LGM) in ICE-5G and then added it to the PMIP3 LGM topography[58]. Global mean sea level is ~80 meters equivalent sea level (m.e.s.l.) lower at 40ka BP than the pre-industrial level. E40ka_CTL is integrated for 5000 years to an equilibrated state that serves as a basis for the following sensitivity experiments.

2. Hosing experiment

The AMOC in E40ka_CTL is in a strong mode. To test whether it is stable we therefore performed a classic North Atlantic (NA) hosing experiment (E40ka_fwf) based on E40ka_CTL (Extended Data Table 1). In E40ka_fwf, freshwater flux by 0.15Sv (1 Sv = 10^6 m^3/s) was imposed into Ruddiman Belt for 500 years to mimic HE4 (i.e. massive iceberg releasing event). Once the hosing was removed at 501st model year, the AMOC recovers abruptly from a weak to a strong mode and remains strong in following 1500 years (Extended Data Fig. 1a). This suggests that the AMOC is in a mono-stable strong mode under the 40ka BP boundary conditions (i.e. in E40ka_CTL). This rules out the previous assertion that freshwater perturbation (i.e. Heinrich Event) might be a potential precondition for the following DOs[8,63].

3. Transient experiment of 40-32ka BP

To test whether orbital changes alone can give rise to millennial-scale climate variability, based on E40ka_CTL we performed a transient experiment by only varying the orbital settings from 40ka to 32ka BP (TRN40ka) (Extended Data Table 1). The imposed orbital parameters are calculated based on Lasker et al (2004)[27] (Fig. 2a, b). Since our focus is on DOs 5-7, we employed an acceleration factor of 10 to simulate the time interval between 40ka BP and 37.5ka BP (i.e. 250 model years represent 2500 calendar years) to accelerate our experiment. The experiment TRN40ka is thus integrated for 5750 model years to represent the time interval between 40 and 32ka BP.

4. Sensitivity experiments under intermediate glacial conditions

To evaluate equilibrium climate responses to certain constant orbital settings, three experiments, E40ka_34kaOrb, E40ka_34kaEP, E40ka_34kaObl, are performed based on E40ka_CTL (same initial ocean state as TRN40ka). In E40ka_34kaOrb, three orbital parameters[27] are set to those at 34ka BP, i.e. eccentricity=0.014996, precession=84.84°, obliquity=22.6°, while the other boundary conditions (e.g. greenhouse gases, ice sheet configuration, etc.) are fixed to E40ka_CTL. In E40ka_34kaObl (E40ka_34kaEP), obliquity (eccentricity-modulated precession) are set to 34ka BP while the rest is identical to E40ka_CTL. E40ka_34kaOrb is integrated for 5500 years to explore the equilibrated responses of glacial climate to the 34ka BP orbital configurations. E40ka_34kaEP and E40ka_34kaObl are integrated for 2000 years since they are mainly used to evaluate whether changes in obliquity or precession alone can account for AMOC oscillations (Extended Data Table 1 and Extended Data Fig. 4, 5).

In E40ka_34kaOrb, we observed the unforced AMOC oscillation with a periodicity of ~1500 years. To evaluate the role of millennial-scale variation in atmospheric CO_2 levels on the unforced oscillation, we performed two sensitivity experiments by instantly increase (E40ka_34kaOrb_pCO2) or decrease (E40ka_34kaOrb_nCO2) CO_2 levels by 10 ppm at the 2050th model year of E40ka_34kaOrb and integrated both of them for 5400 years to assess their equilibrium responses to these CO_2 changes. In both experiments, spontaneous DO-like AMOC oscillations were sustained, indicating that millennial-scale CO_2 variability (~20 ppm) cannot shift the AMOC out of the window of its oscillating regime (Fig. 4). This is likely due to that atmospheric CO_2 changes from 205 to 185 ppm are equivalent to changes in radiative forcing of ~0.55 W/m^2 [64], which are too weak to overcome the impacts of insolation changes. Nevertheless, these changes can alter the thermohaline balance between the low- and high-latitude NA[12], affecting the timing characteristics of the oscillations. That is, decreasing atmospheric CO_2 is capable of reducing interstadial durations, thereby shortening the oscillating periodicity (Fig. 4). During MIS3, durations of warm interstadials have a close relationship with Antarctic/Southern Ocean temperatures, which shares a close correspondence with changes in atmospheric CO_2[5,7,65]. For instance, the successive DOs 5-7 have a decreasing interstadial duration along with a cooling background associated with a gradual CO_2 decline of ~15 ppm[5,7,8,25,65]. Therefore, these results, in addition to the notion that changes in the AMOC and associated global response are thought to alter atmospheric CO_2 levels, suggest that millennial-scale CO_2 changes may serve as an internal

climate agent modulating timing characteristics of millennial-scale climate variability during glacial periods.

To evaluate the role of millennial-scale changes in global mean sea level during MIS3, we instantly altered the ice sheet configuration of 40ka BP to that of 50ka BP at the 2050th model year of E40ka_34kaOrb and integrated it for 3200 model years (E40ka_34kaOrb_50kaICE). Note that the way of generating 50ka BP ice sheet configuration is identical to that of 40ka BP. The ice volume at 50ka BP is ~ 12.5 m.s.l.e. lower than 40ka BP according to ICE-5G[62]. In this 3200-year experiment, the AMOC shifts from its stable oscillating mode to a stable weak mode, indicating the important role of ice-sheet changes in altering the oscillating properties (Phase A in Fig. 5). This is due to the associated changes in atmospheric circulation[7,59], which on one hand enhances sea ice transport from the Labrador Sea to the key convection sites and on the other hand weakens the subtropical gyre to transport warm and salty water northwards. This alters the tropical and subpolar thermohaline balances in the North Atlantic in E40ka_34kaOrb, resulting in a weak AMOC mode under a lower ice-volume configuration with the same orbital forcing to E40ka_34kaOrb.

According to the governing mechanisms of unforced AMOC oscillation, it is likely that increasing obliquity and eccentricity-modulated precession (opposite to orbital changes from 40ka to 34ka BP) can restart AMOC self-oscillations under the low ice-volume configuration (Phase A in Fig. 5). Therefore, we performed an experiment (E40ka_50kaICE) by instantly imposing 40ka BP orbital configurations in E40ka_34kaOrb_50kaICE (i.e. at the 5250th model year as shown in Fig. 5) for 5400 model years. As expected, the AMOC oscillating mode was reinitiated (Phase B in Fig. 5). Notably, these oscillations in E40ka_50kaICE are not characterized by the classic 'sawtooth'-like variation (i.e. relatively stable stadial with occasional returns to interstadial conditions). This is attributed to the lowered Northern Hemisphere ice volume, of which impacts on the tropical and subpolar thermohaline balance in the North Atlantic remains dominant, resulting in a state in which the weak AMOC phase is relatively stable under 40ka BP orbital configurations. Changing the orbital settings further back to 50ka BP – a period with higher obliquity and precession than those during 40ka BP – produces a return of the classic 'sawtooth'-like AMOC oscillation (Phase C in Fig. 5). These stepwise transient experiments as shown in Fig. 5 corroborate the governing role of orbital changes in unforced AMOC oscillatory regime under various intermediate ice sheet configurations.

5. Sensitivity experiments under peak interglacial and glacial maximum conditions

Previous studies have proposed that changes in internal climate backgrounds can control the sensitivity of the AMOC to applied perturbations[9,10,12,19]. In particular, high atmospheric CO_2 levels during peak interglacials and high Northern Hemisphere ice sheets during glacial maxima will give rise to a very stable AMOC with a high resistance to additional internal climate perturbations. To test whether this assertion holds for insolation changes, we therefore designed a set of orbital sensitivity experiments under the Last Glacial Maximum (LGM) or Pre-industrial (PI) conditions by applying extreme orbital settings of the last 2 million years. That is, eccentricity-modulated precession is set to either -0.04 or 0.04 and obliquity is set to either 22° or 24.5°. This results in four different sensitivity experiments under each boundary conditions (Extended Data Table 1). We integrated each experiment for 1500 years to ensure a quasi-equilibrium climate. As inferred, no AMOC mode transitions occur in these runs (Extended Data Fig. 7), confirming the previous assertion about the dominant roles of atmospheric CO_2 and Northern Hemisphere ice sheet height on AMOC stability.

6. Experiments in Atmospheric General Circulation Model

Present-day observations suggest that changes in Atlantic Warm Pool intensity play a significant role on the mean Atlantic-to-Pacific moisture export[30]. That is, an enhanced and expanded Atlantic Warm Pool reduces moisture export by stimulating anomalous convergent flow and weak trade wind in the North Atlantic[30]. This, in addition to the notion that the Atlantic Warm Pool mainly appears during boreal summer[66], indicates that Earth's precession can modulate mean hydrology cycles in the tropical NA via the impacts of summer insolation on Atlantic Warm Pool intensity. To confirm this inference and associated dynamics at precessional timescale, we conducted a series of sensitivity experiment in an atmospheric general circulation model (AGCM), ECHAM5. The key goal of the AGCM experiments is to explore equilibrated climate responses to precession change and associated dynamics under conditions without evident change in the AMOC. This can largely minimize the uncertainty caused by ocean processes adjusting to an oscillatory AMOC mode. The AMOC under the LGM conditions is always in a stable strong mode even if applying extreme summer insolation changes by shifting Earth's position from aphelion (LGM_Hobl_LSea) to perihelion (LGM_Hobl_HSea) during boreal summer solstice, unlike the cases under the 40ka BP conditions (E40ka_CTL and E40ka_34kaEP). Therefore, we employ the results from these

precessional sensitivity experiments under LGM conditions. The experimental ID with prefix "A_" represents AGCM experiments to distinguish experiments in coupled climate model. Each AGCM experiment is integrated for 50 years, and the average of the last 30 years is used to represent the corresponding climatology.

To first confirm the AGCM can capture climate responses derived from the coupled model, we conducted two experiments, A_CTL and A_ORB_SST, by applying full forcing (i.e. SST, SIC and orbital settings) from LGM_Hobl_LSea and LGM_Hobl_HSea, respectively. In line with results from coupled model (Extended Data Fig. 6a), the AGCM results well reproduce the key features of climate response to boreal summer insolation increase (Extended Data Fig. 6b). All other AOGCM experiments are all based on the settings in A_CTL, unless specified differently. To assess contributions of terrestrial and oceanic responses to overall climate responses in A_ORB_SST, we conducted two experiments, A_ORB and A_SST, by applying either orbital settings or SST and SIC from LGM_Hobl_HSea, respectively. Note that applying the orbital settings alone only causes terrestrial temperature change in AGCM. As shown in Extended Data Fig 7c and d, only applying oceanic changes can the AGCM reproduce similar climate response to A_ORB_SST (Extended Data Fig. 6b). Accordingly, we performed an experiment directly relevant to our hypothesis, A_TroNASST, by only imposing the SST changes in subtropical North Atlantic where Atlantic Warm Pool locates (Extended Data Fig. 6e). It appears that A_TroNASST can well reproduce the enhanced net precipitation by trapping more moisture in the North Atlantic, similar to that in A_ORB_SST and A_SST. Together with experiment A_ORB_EPSST in which orbital settings and SST changes are only applied in equatorial eastern Pacific (Extended Data Fig. 7f), this substantiates that precessional changes in Atlantic Warm Pool intensity do play a dominant role in hydrology change in the North Atlantic.

Data-model comparison

Model-data comparison is a valuable approach to analyze both the simulated model results and proxy-based reconstructions. During the glacial-interglacial cycles of the last 800ka BP, MIS3 is characterized with the most abundance of proxy records that are able to resolve MCV globally[67]. Here we compare our model results with 44 published proxy records (Extended Data Table 2-3), to qualitatively assess the reliability of the simulated spontaneous AMOC oscillation (AMOC instability) for explaining MCV under intermediate glacial conditions (Extended Data Fig. 3).

As shown in Extended Data Fig. 2a-b and f-g, it is evident that the abrupt warming in the Northern Hemisphere is in concert with a rapid AMOC transition with latitudinal shifts of the main convection sites (not shown), consistent with the inferences derived from $\delta^{13}C$ and magnetic records for DO events during MIS3 (e.g. ref. [68,69]). Along with abrupt AMOC transition from its weak to strong phase, significant changes in global precipitation and surface temperature patterns are also well recorded in a variety of global proxy datasets (Extended Data Fig. 3, Table 2, 3). In both TRN40ka and E40ka_34kaOrb, the Atlantic bipolar thermal seesaw, which is clearly documented in paleoclimate reconstructions from the North and South Atlantic (e.g. ref. [67,70,71]), is generally captured in our model simulations (Extended Data Fig. 3a, c). Our model simulates the global and regional responses of surface temperature to AMOC change very well, although underestimates the warming magnitudes especially over the Greenland, which can be potentially attributed to underestimation of sea-ice responses in the Nordic Sea to the AMOC change[10,72]. The Intertropical Convergence Zone (ITCZ) shifts northward as Northern Hemisphere warming occurs, as indicated by proxy data (Extended Data Fig. 3b, d). In response to the enhanced AMOC, increased water vapor is transported further northward from the mid latitudes to high latitudes in the North Atlantic, leading to a drying phase over the subtropics (e.g. mid Florida)[73] and a wet phase over the North-East Atlantic (e.g. Europe)[74]. The northern warming also strengthens Asian summer monsoon, which are characterized with evident increase in precipitation. In conclusion, the two AMOC phases in the AMOC oscillatory regime with respect to orbital changes can well capture key features of DO events (e.g. ref. [67,70]), adding credibility to our proposed mechanism for explaining abrupt climate shifts during intermediate glacial conditions.

Atlantic meridional salinity transport

To diagnose the meridional salinity transport associated with AMOC, M_{ov}, across the boundary between NA subpolar and subtropical gyre (~43°N), we follow the equation that is widely used to evaluate freshwater import or export across the southern boundary of the Atlantic (e.g. [75]) by reversing its sign. The equation used here is as follows:

$$M_{ov} = \frac{1}{S_0} \int dz\, \overline{v}(z)\, [\langle S(z) \rangle - S_0]$$

where S_0 is Atlantic mean salinity value; the overbar and the angle brackets $\langle \cdot \rangle$ denote zonal integration and zonal averaging along one latitude, respectively.

Data availability: The paleoclimate records used in this paper are available at the following sources. Lisiecki and Raymo 2005, benthic $\delta^{18}O$ stack: https://doi.pangaea.de/10.1594/PANGAEA.704257, Bereiter *et al.* (2015), CO_2 data: http://onlinelibrary.wiley.com/store/10.1002/2014GL061957/asset/supinfo/grl52461-sup-0003-supplementary.xls?v=1&s= e77ad89c3925111330671009ab40eac65e019d01. Barker et al (2019), ODP983 NPS data: https://doi.pangaea.de/10.1594/PANGAEA.904398. The model data that supports the key findings of this study are available in National Tibetan Plateau Data Center (TPDC) with doi: 10.11888/Paleoenv.tpdc.271670.

Code availability: The standard model code of the 'Community Earth System Models' (COSMOS) version COSMOS-landveg r2413 (2009) is available upon request from the 'Max Planck Institute for Meteorology' in Hamburg (https://www.mpimet.mpg.de). Post-processing of model output and model data analysis has been performed with CDO (Climate Data Operators, version 1.9.5 and 1.9.10, https://code.mpimet.mpg.de/projects/cdo).

Correspondence and requests for materials should be addressed to X.Z.

Additional References for Method Section:

51. Grinsted, A., Moore, J. C. & Jevrejeva, S. Application of the cross wavelet transform and wavelet coherence to geophysical time series. *Nonlinear Process. Geophys.* (2004) doi:10.5194/npg-11-561-2004.

52. Roeckner, E. *et al.* The atmospheric general circulation model ECHAM5: Part 1: Model description. *MPI Rep.* 1–140 (2003) doi:10.1029/2010JD014036.

53. Brovkin, V., Raddatz, T., Reick, C. H., Claussen, M. & Gayler, V. Global biogeophysical interactions between forest and climate. *Geophys. Res. Lett.* **36**, 1–5 (2009).

54. Marsland, S. J., Haak, H., Jungclaus, J. H., Latif, M. & Röske, F. The Max-Planck-Institute global ocean/sea ice model with orthogonal curvilinear coordinates. *Ocean Model.* **5**, 91–127 (2003).

55. Hibler III, W. A dynamic thermodynamic sea ice model. *J. Phys. Oceanogr.* **9**, 815–846 (1979).

56. Wei, W. & Lohmann, G. Simulated Atlantic Multidecadal Oscillation during the Holocene. *J. Clim.* **25**, 6989–7022 (2012).

57. Gong, X., Knorr, G., Lohmann, G. & Zhang, X. Dependence of abrupt Atlantic meridional ocean circulation changes on climate background states. *Geophys. Res. Lett.* **40**, 3698–3704 (2013).

58. Zhang, X., Lohmann, G., Knorr, G. & Xu, X. Different ocean states and transient characteristics in Last Glacial Maximum simulations and implications for deglaciation. *Clim. Past* **9**, 2319–2333 (2013).

59. Knorr, G. & Lohmann, G. Climate warming during Antarctic ice sheet expansion at the Middle Miocene transition. *Nat. Geosci.* **7**, 2–7 (2014).

60. Stärz, M., Jokat, W., Knorr, G. & Lohmann, G. Threshold in North Atlantic-Arctic Ocean circulation controlled by the subsidence of the Greenland-Scotland Ridge. *Nat. Commun.* **8**, 1–13 (2017).

61. Köhler, P., Nehrbass-Ahles, C., Schmitt, J., Stocker, T. F. & Fischer, H. A 156 kyr smoothed history of the atmospheric greenhouse gases CO 2 , CH 4 , and N 2 O and their radiative forcing. *Earth Syst. Sci. Data* **95194**, 363–387 (2017).

62. Peltier, W. R. Global Glacial Isostasy and the Surface of the Ice-Age Earth : The ICE-5G (VM2) Model and GRACE. *Annu. Rev. Earth Planet. Sci.* **32**, 111–149 (2004).

63. Hemming, S. Heinrich Events: Massive Late Pleistocene Detritus Layers of the North Atlantic and their global Climate Imprint. *Rev. Geophys.* **42**, RG1005 (2004).

64. Myhre, G., Highwood, E. J., Shine, K. P. & Stordal, F. New estimates of radiative forcing due to well mixed greenhouse gases. *Geophys. Res. Lett.* **25**, 2715–2718 (1998).

65. Bereiter, B. *et al.* Revision of the EPICA Dome C CO2 record from 800 to 600 kyr before present. *Geophys. Res. Lett.* **42**, 1–8 (2015).

66. Wang, C., Enfield, D. B., Lee, S. K. & Landsea, C. W. Influences of the Atlantic warm pool on western hemisphere summer rainfall and Atlantic hurricanes. *J. Clim.* **19**, 3011–3028 (2006).

67. Voelker, A. H. L. Global distribution of centennial-scale records for Marine Isotope Stage (MIS) 3: a database. *Quat. Sci. Rev.* **21**, 1185–1212 (2002).

68. Kissel, C., Laj, C., Labeyrie, L. & Dokken, T. Rapid climatic variations during marine isotopic stage 3: Magnetic analysis of sediments from Nordic Seas and North Atlantic. *Earth Planet. Sci. Lett.* **171**, 489–502 (1999).

69. Elliot, M., Labeyrie, L. & Duplessy, J. Changes in North Atlantic deep-water formation associated with the Dansgaard – Oeschger temperature oscillations (60 – 10 ka). *Quat. Sci. Rev.* **21**, 1153–1165 (2002).

70. Barbante, C. *et al.* One-to-one coupling of glacial climate variability in Greenland and Antarctica. *Nature* **444**, 195–198 (2006).

71. Barker, S. *et al.* Interhemispheric Atlantic seesaw response during the last deglaciation. *Nature* **457**, 1097–102 (2009).

72. Li, C., Battisti, D. S. & Bitz, C. M. Can North Atlantic Sea Ice Anomalies Account for Dansgaard–Oeschger Climate Signals?*. *J. Clim.* **23**, 5457–5475 (2010).

73. Grimm, E. C. *et al.* Evidence for warm wet Heinrich events in Florida. *Quat. Sci. Rev.* **25**, 2197–2211 (2006).

74. Van Meerbeeck, C. J. *et al.* The nature of MIS 3 stadial–interstadial transitions in Europe: New insights from model–data comparisons. *Quat. Sci. Rev.* **30**, 3618–3637 (2011).

75. Weber, S. L. *et al.* The modern and glacial overturning circulation in the Atlantic ocean in PMIP coupled model simulations. *Clim. Past* **3**, 51–64 (2007).

76. Grootes, P. M., Stulver, M., White, J. W. C., Johnsen, S. & Jouzel, J. Comparison of Oxygen isotope records from the GISP2 and GRIP Greenland ice cores. *Nature* **366**, 552–554 (1993).

77. Huber, C. *et al.* Isotope calibrated Greenland temperature record over Marine Isotope Stage 3 and its relation to CH4. *Earth Planet. Sci. Lett.* **243**, 504–519 (2006).

78. Rasmussen, T. L. & Thomsen, E. Warm Atlantic surface water inflow to the Nordic seas 34-10 calibrated ka B.P. *Paleoceanography* **23**, PA1201 (2008).

79. Rasmussen, T., Thomsen, E., Labeyriefi, L. & van Weering, T. C. E. Circulation changes in the Faeroe-Shetland Channel correlating with cold events during the last glacial period (58–10 ka). *Geology* **24**, 937–940 (1996).

80. Rasmussen, T., Thomsen, E., Troelstra, S. R., Kuijpers, A. & Prins, M. a. Millennial-scale glacial variability versus Holocene stability: changes in planktic and benthic foraminifera faunas and ocean circulation in the North Atlantic during the last 60 000 years. *Mar. Micropaleontol.* **47**, 143–176 (2002).

81. Rasmussen, T. L. *et al.* The Faroe-Shetland Gateway : Late Quaternary water mass exchange between the Nordic seas and the northeastern Atlantic. *Mar. Geol.* **188**, 165–192 (2002).

82. Kandiano, E. S., Bauch, H. a. & Müller, a. Sea surface temperature variability in the North Atlantic during the last two glacial–interglacial cycles: comparison of faunal, oxygen isotopic, and Mg/Ca-derived records. *Palaeogeogr. Palaeoclimatol. Palaeoecol.* **204**, 145–164 (2004).

83. Kiefer, T., Sarnthein, M., Erlenkeuser, H., Grootes, P. M. & Roberts, A. P. North Pacific response to millennial-scale changes in ocean circulation over the last 60 kyr. *Paleoceanography* **16**, 179–189 (2001).

84. Harada, N. *et al.* Rapid fluctuation of alkenone temperature in the southwestern Okhotsk Sea during the past 120 ky. *Glob. Planet. Change* **53**, 29–46 (2006).

85. Martrat, B. *et al.* Four Climate Cycles of Recurring Deep and Surface Water Destabilizations on the Iberian Margin. *Science (80-.).* **317**, 502–507 (2007).

86. Cacho, I., Grimalt, J. & Pelejero, C. Dansgaard-Oeschger and Heinrich event imprints in Alboran Sea paleotemperatures. *Paleoceanography* **14**, 698–705 (1999).

87. Hendy, I. & Kennett, J. Dansgaard-Oeschger cycles and the California Current System: Planktonic foraminiferal response to rapid climate change in Santa Barbara Basin , Ocean Drilling Program hole 893A. *Paleoceanography* **15**, 30–42 (2000).

88. Sachs, J. P. & Lehmann, S. J. Subtropical North Atlantic Temperatures 60,000 to 30,000 Years Ago. *Science (80-.).* **286**, 756–759 (1999).

89. Simon, M. H. *et al.* Millennial-scale Agulhas Current variability and its implications for salt-leakage through the Indian–Atlantic Ocean Gateway. *Earth Planet. Sci. Lett.* **383**, 101–112 (2013).

90. Lamy, F. *et al.* Antarctic timing of surface water changes off Chile and Patagonian ice sheet response. *Science* **304**, 1959–1962 (2004).

91. Pahnke, K., Zahn, R., Elderfield, H. & Schulz, M. 340000 year Centennial-scale Marine Record of Southern Hemisphere Climatic Oscillation. *Science (80-.).* **301**, 948–952 (2003).

92. Caniupán, M. *et al.* Millennial-scale sea surface temperature and Patagonian Ice Sheet changes off southernmost Chile (53°S) over the past ~60 kyr. *Paleoceanography* **26**, PA3221 (2011).

93. Augustin, L. *et al.* Eight glacial cycles from an Antarctic ice core. *Nature* **429**, 623–8 (2004).

94. Blunier, T. & Brook, E. J. Timing of millennial-scale climate change in Antarctica and Greenland during the last glacial period. *Science* **291**, 109–12 (2001).

95. Müller, U. C. *et al.* The role of climate in the spread of modern humans into Europe. *Quat. Sci. Rev.* **30**, 273–279 (2011).

96. Wang, Y. J. *et al.* A high-resolution absolute-dated late Pleistocene Monsoon record from Hulu Cave, China. *Science (80-.).* **294**, 2345–2348 (2001).

97. Bar-Matthews, M., Ayalon, A., Gilmour, M., Matthews, A. & J., H. C. Sea–land oxygen isotopic relationships from planktonic foraminifera and speleothems in the Eastern Mediterranean region and their implication for paleorainfall during interglacial intervals. *Geochim. Cosmochim. Acta* **67**, 3181–3199 (2003).

98. Yuan, D. *et al.* Timing, duration, and transitions of the last interglacial Asian monsoon. *Science (80-.).* **304**, 575–8 (2004).

99. Schulz, H., Rad, U. von & Erlenkeuser, H. Correlation between Arabian Sea and Greenland climate oscillations of the past 110,000 years. *Nature* **393**, 23–25 (1998).

100. Altabet, M., Higginson, M. & Murray, D. The effect of millennial-scale changes in Arabian Sea denitrication on atmospheric CO2. *Nature* **764**, 159–162 (2002).

101. Hodell, D. a. *et al.* An 85-ka record of climate change in lowland Central America. *Quat. Sci. Rev.* **27**, 1152–1165 (2008).

102. Burns, S. J., Fleitmann, D., Matter, A., Kramers, J. & Al-Subbary, A. a. Indian Ocean climate and an absolute chronology over Dansgaard/Oeschger events 9 to 13. *Science (80-.).* **301**, 1365–1367 (2003).

103. Peterson, L. C., Haug, G. H., Hughen, K. A. & Roehl, U. Rapid Changes in the Hydrologic Cycle of the Tropical Atlantic During the Last Glacial. *Science (80-.).* **290**, 1947–1951 (2000).

104. Tierney, J. E. *et al.* Northern hemisphere controls on tropical southeast African climate during the past 60,000 years. *Science (80-.).* **322**, 252–255 (2008).

105. Brown, E. T., Johnson, T. C., Scholz, C. a., Cohen, a. S. & King, J. W. Abrupt change in tropical African climate linked to the bipolar seesaw over the past 55,000 years. *Geophys. Res. Lett.* **34**, L20702 (2007).

106. Wang, X. *et al.* Wet periods in northeastern Brazil over the past 210 kyr linked to distant climate anomalies. *Nature* **432**, 740–743 (2004).

107. Kanner, L. C., Burns, S. J., Cheng, H. & Edwards, R. L. High-latitude forcing of the South American summer monsoon during the Last Glacial. *Science (80-.).* **335**, 570–573 (2012).

108. Turney, C., Kershaw, A. & Clemens, S. Millennial and orbital variations of El Nino/Southern Oscillation and high-latitude climate in the last glacial period. *Nature* **428**, 306–310 (2004).

109. Baker, P. a *et al.* Tropical climate changes at millennial and orbital timescales on the Bolivian Altiplano. *Nature* **409**, 698–701 (2001).

110. Cruz, F. W., Burns, S. J., Karmann, I., Sharp, W. D. & Vuille, M. Reconstruction of regional atmospheric circulation features during the late Pleistocene in subtropical Brazil

from oxygen isotope composition of speleothems. *Earth Planet. Sci. Lett.* **248**, 495–507 (2006).

111. Wang, X. *et al.* Interhemispheric anti-phasing of rainfall during the last glacial period. *Quat. Sci. Rev.* **25**, 3391–3403 (2006).

112. Cruz Jr, F. W. *et al.* Insolation-driven changes in atmospheric circulation over the last 116000 years in subtropical Brazil. *Nature* **434**, 63–66 (2005).

113. Ziegler, M. *et al.* Development of Middle Stone Age innovation linked to rapid climate change. *Nat. Commun.* **4**, 1905 (2013).

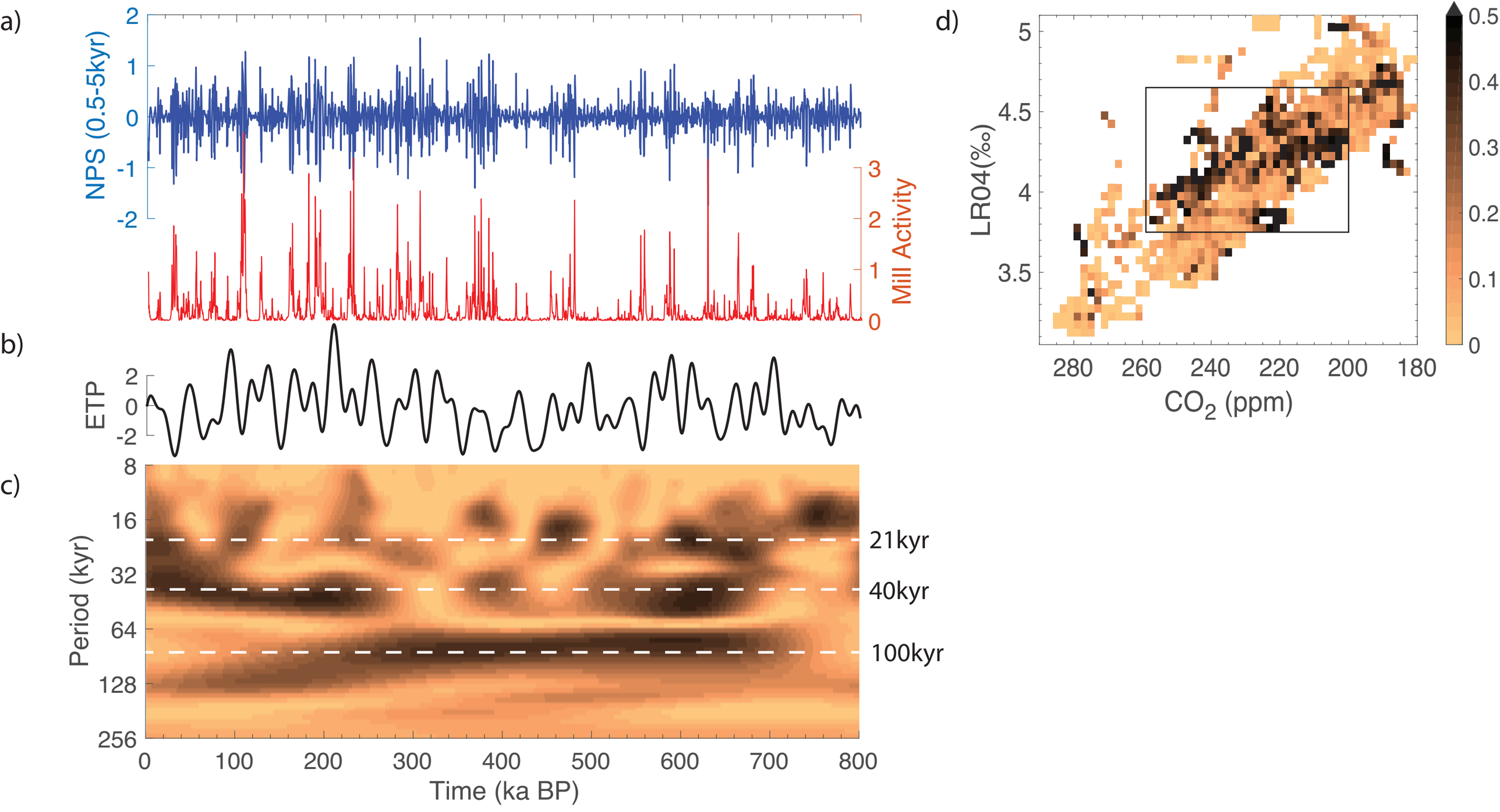
a)
NPS (0.5-5kyr)
Mill Activity
b)
ETP
c)
Period (kyr)
21kyr
40kyr
100kyr
Time (ka BP)
d)
LR04(‰)
CO2 (ppm)

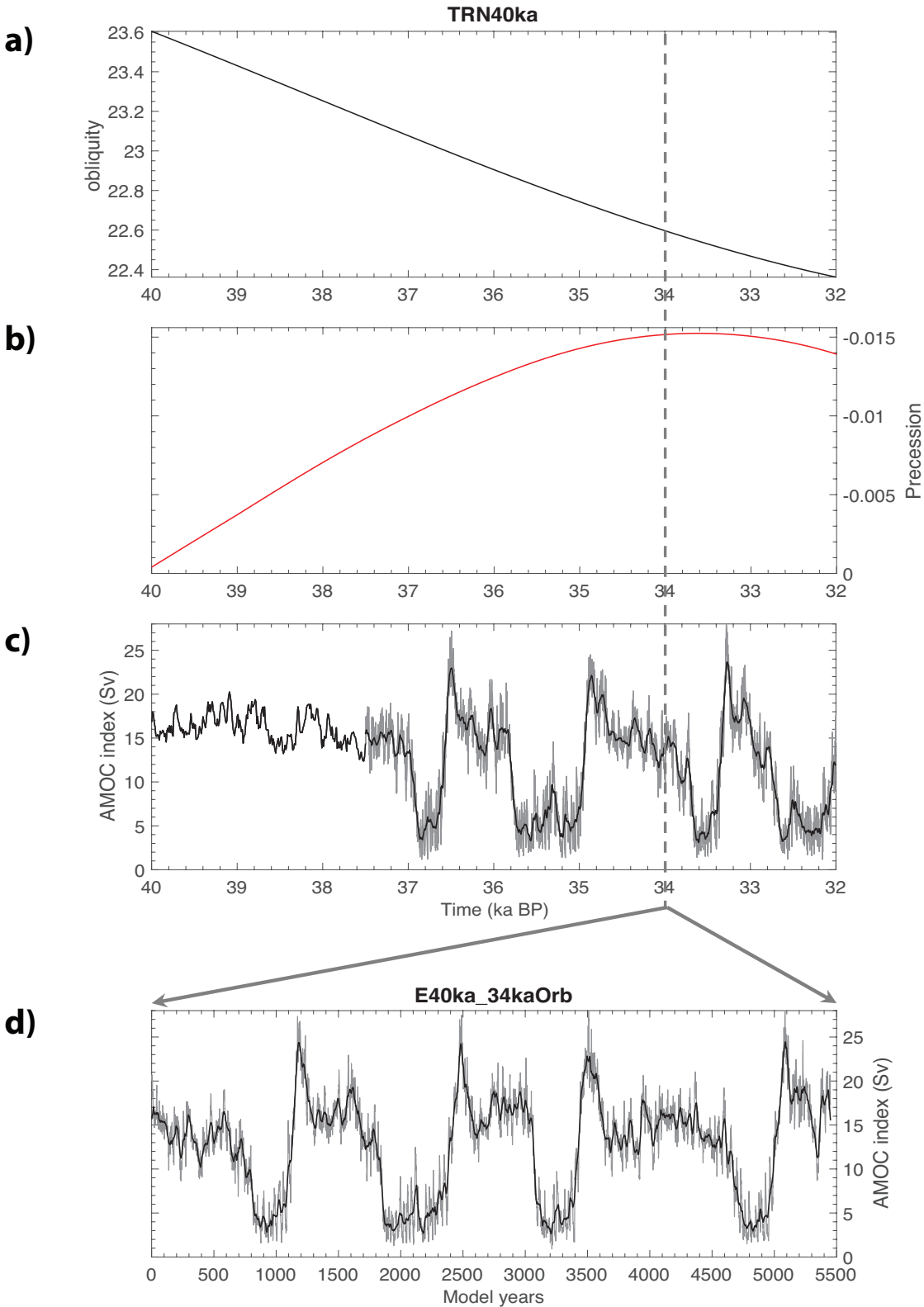
a)
TRN40ka
obliquity
23.6
23.4
23.2
23
22.8
22.6
22.4
40
39
38
37
36
35
34
33
32
b)
-0.015
-0.01
-0.005
0
Precession
c)
AMOC index (Sv)
25
20
15
10
5
0
Time (ka BP)
d)
E40ka_34kaOrb
AMOC index (Sv)
0
500
1000
1500
2000
2500
3000
3500
4000
4500
5000
5500
Model years

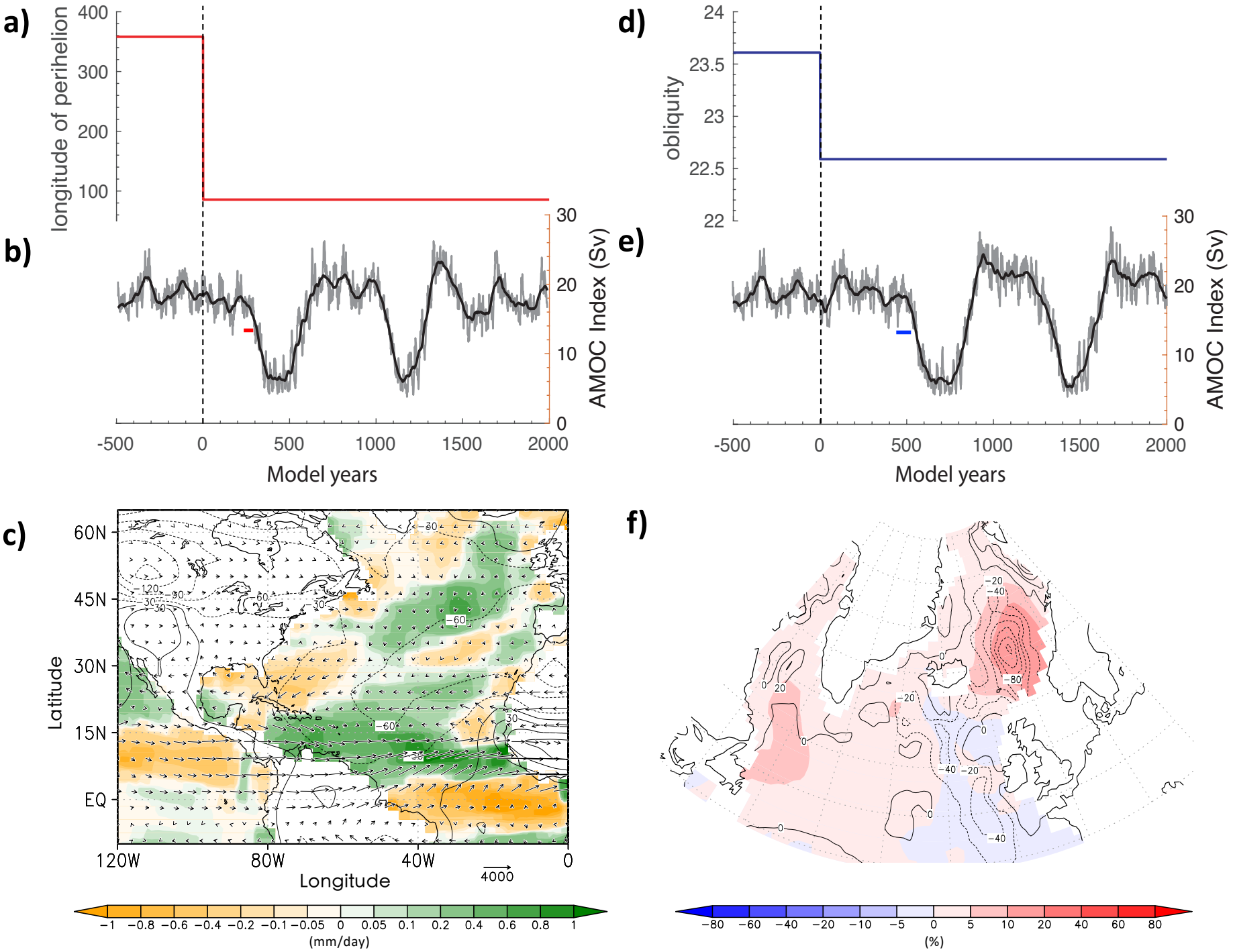
a)
b)
c)
d)
e)
f)
longitude of perihelion
AMOC Index (Sv)
Model years
obliquity
Latitude
Longitude
60N
45N
30N
15N
EQ
120W
80W
40W
0
4000
(mm/day)
(%)

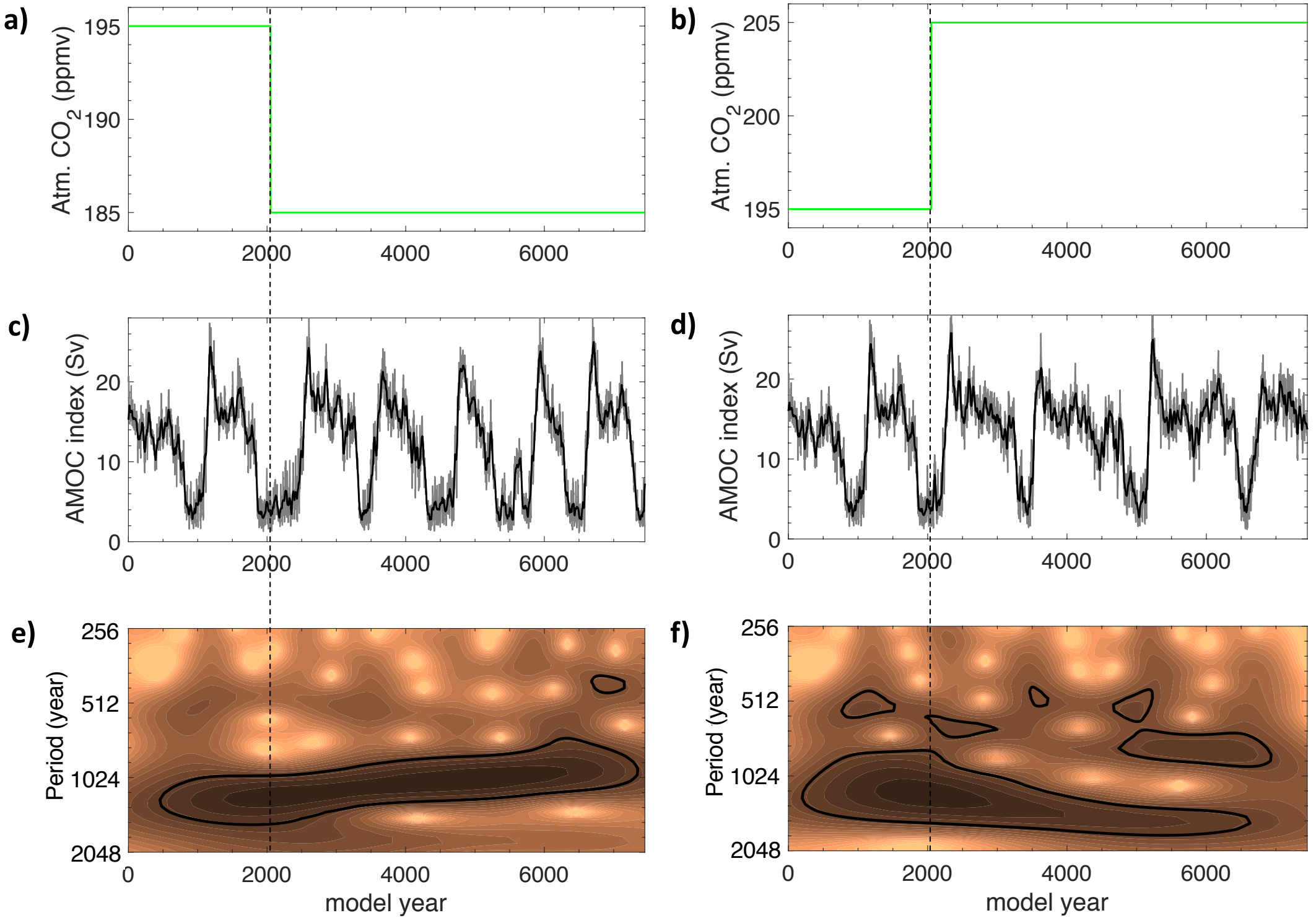
a)
b)
c)
d)
e)
f)
Atm. CO2 (ppmv)
195
190
185
205
200
AMOC index (Sv)
20
10
0
2000
4000
6000
Period (year)
256
512
1024
2048
model year

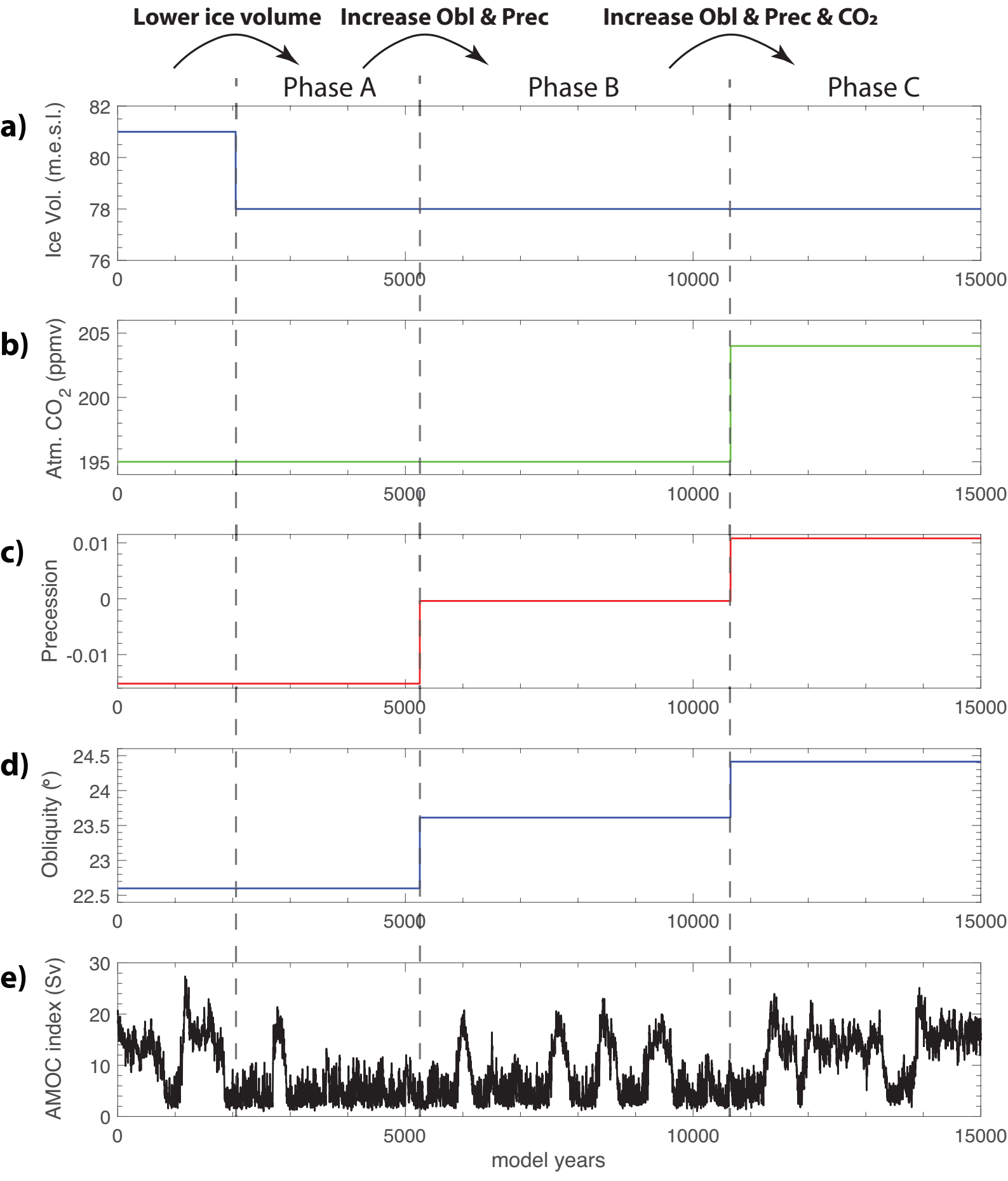
Lower ice volume
Increase Obl & Prec
Increase Obl & Prec & CO₂
Phase A
Phase B
Phase C
a)
Ice Vol. (m.e.s.l.)
82
80
78
76
b)
Atm. CO2 (ppmv)
205
200
195
c)
Precession
0.01
0
-0.01
d)
Obliquity (°)
24.5
24
23.5
23
22.5
e)
AMOC index (Sv)
30
20
10
0
0
5000
10000
15000
model years

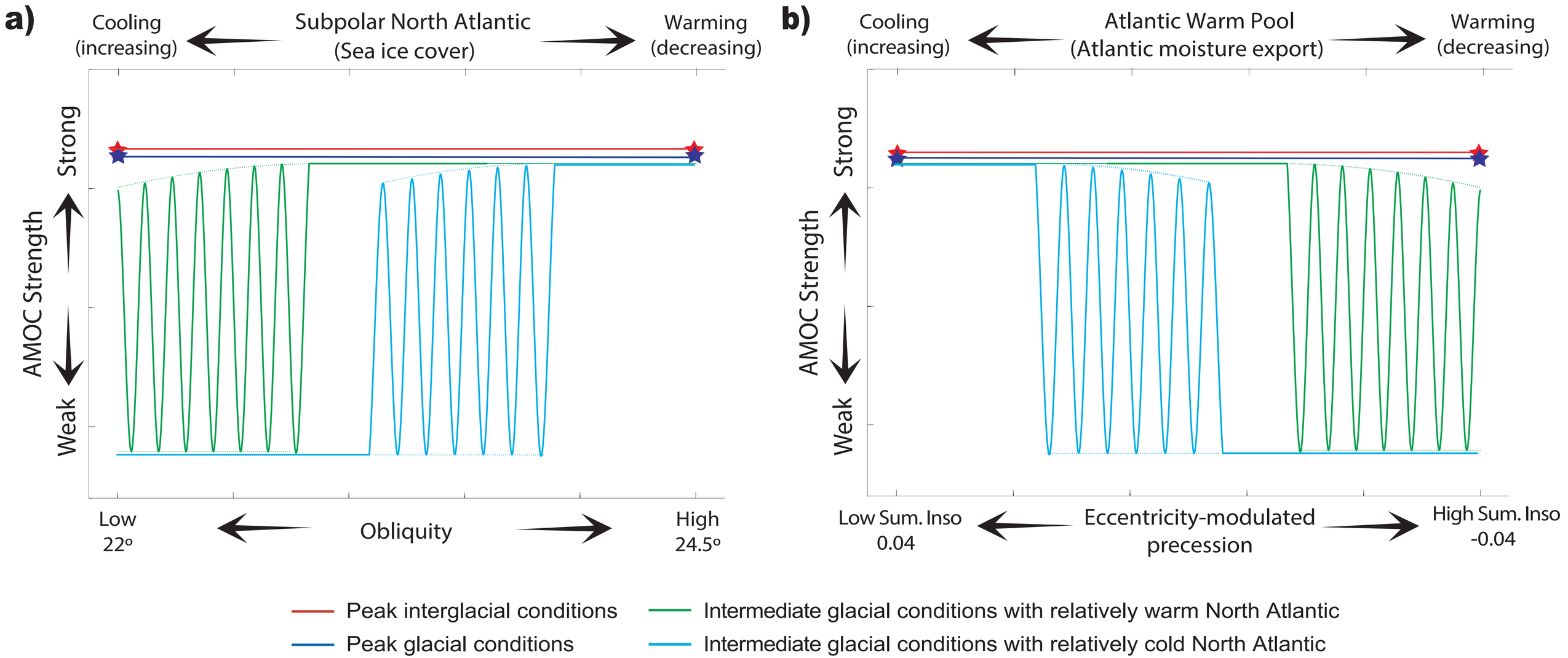
a)
Cooling (increasing)
Subpolar North Atlantic (Sea ice cover)
Warming (decreasing)
AMOC Strength
Strong
Weak
Low 22°
Obliquity
High 24.5°
b)
Cooling (increasing)
Atlantic Warm Pool (Atlantic moisture export)
Warming (decreasing)
AMOC Strength
Strong
Weak
Low Sum. Inso 0.04
Eccentricity-modulated precession
High Sum. Inso -0.04
Peak interglacial conditions
Peak glacial conditions
Intermediate glacial conditions with relatively warm North Atlantic
Intermediate glacial conditions with relatively cold North Atlantic

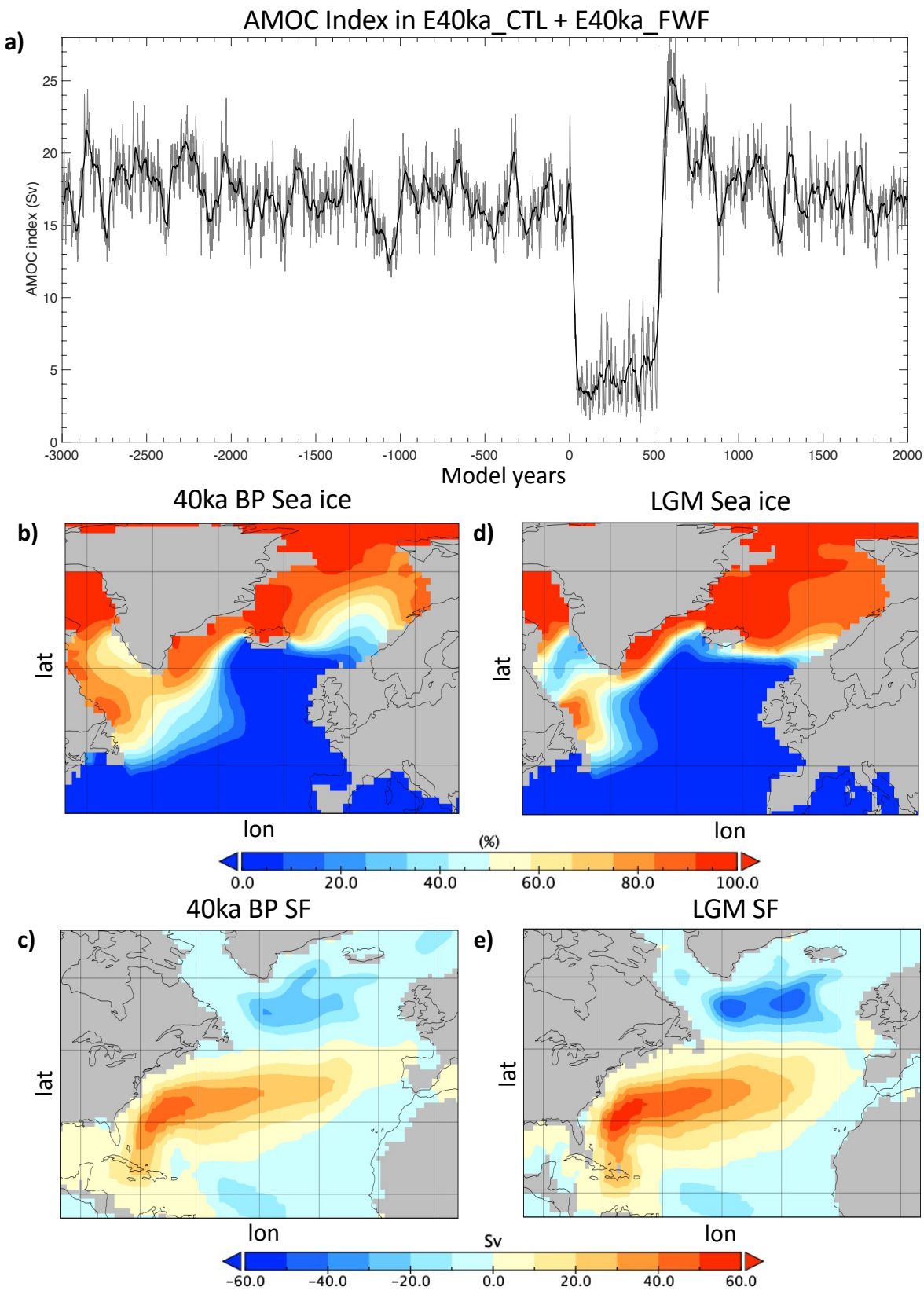
a)
AMOC Index in E40ka_CTL + E40ka_FWF
AMOC index (Sv)
Model years
b)
40ka BP Sea ice
d)
LGM Sea ice
lat
lon
(%)
0.0
20.0
40.0
60.0
80.0
100.0
c)
40ka BP SF
e)
LGM SF
Sv
-60.0
-40.0
-20.0
0.0
20.0
40.0
60.0

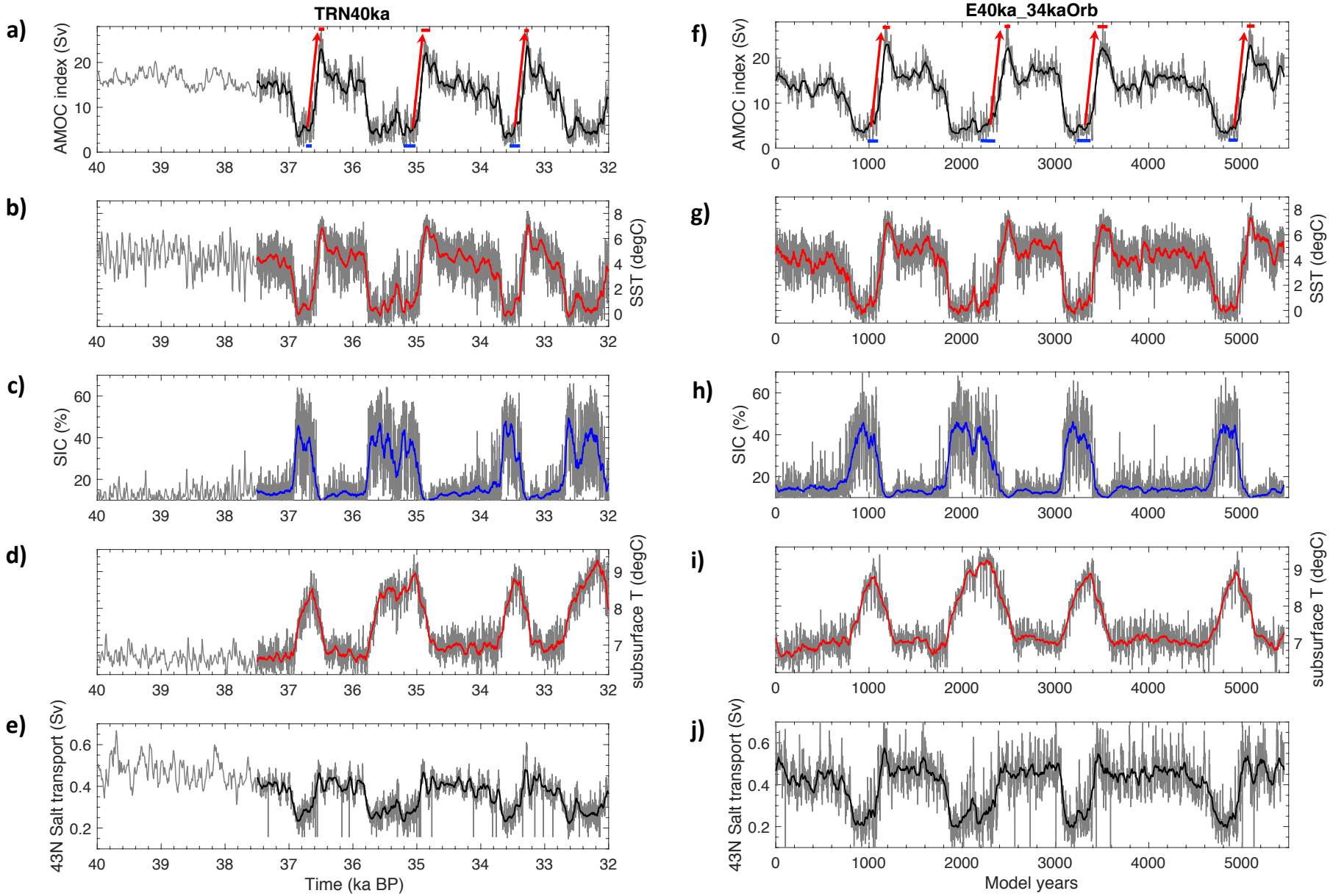
a)
TRN40ka
AMOC index (Sv)
b)
SST (degC)
c)
SIC (%)
d)
subsurface T (degC)
e)
43N Salt transport (Sv)
Time (ka BP)
f)
E40ka_34kaOrb
AMOC index (Sv)
g)
SST (degC)
h)
SIC (%)
i)
subsurface T (degC)
j)
43N Salt transport (Sv)
Model years

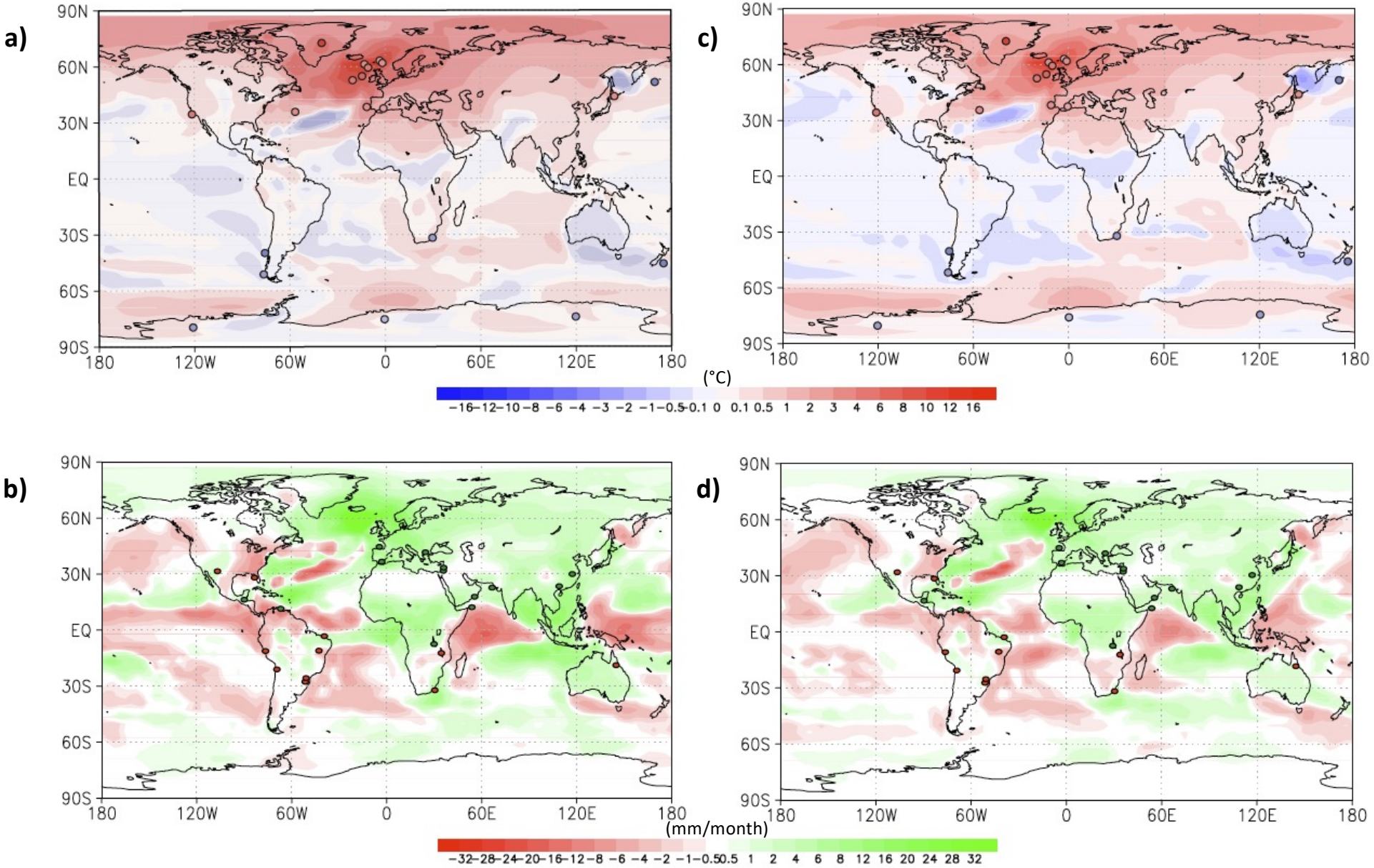
a)
c)
b)
d)
90N
60N
30N
EQ
30S
60S
90S
180
120W
60W
0
60E
120E
180
(°C)
−16 −12 −10 −8 −6 −4 −3 −2 −1 −0.5 −0.1 0 0.1 0.5 1 2 3 4 6 8 10 12 16
(mm/month)
−32 −28 −24 −20 −16 −12 −8 −6 −4 −2 −1 −0.5 0.5 1 2 4 6 8 12 16 20 24 28 32

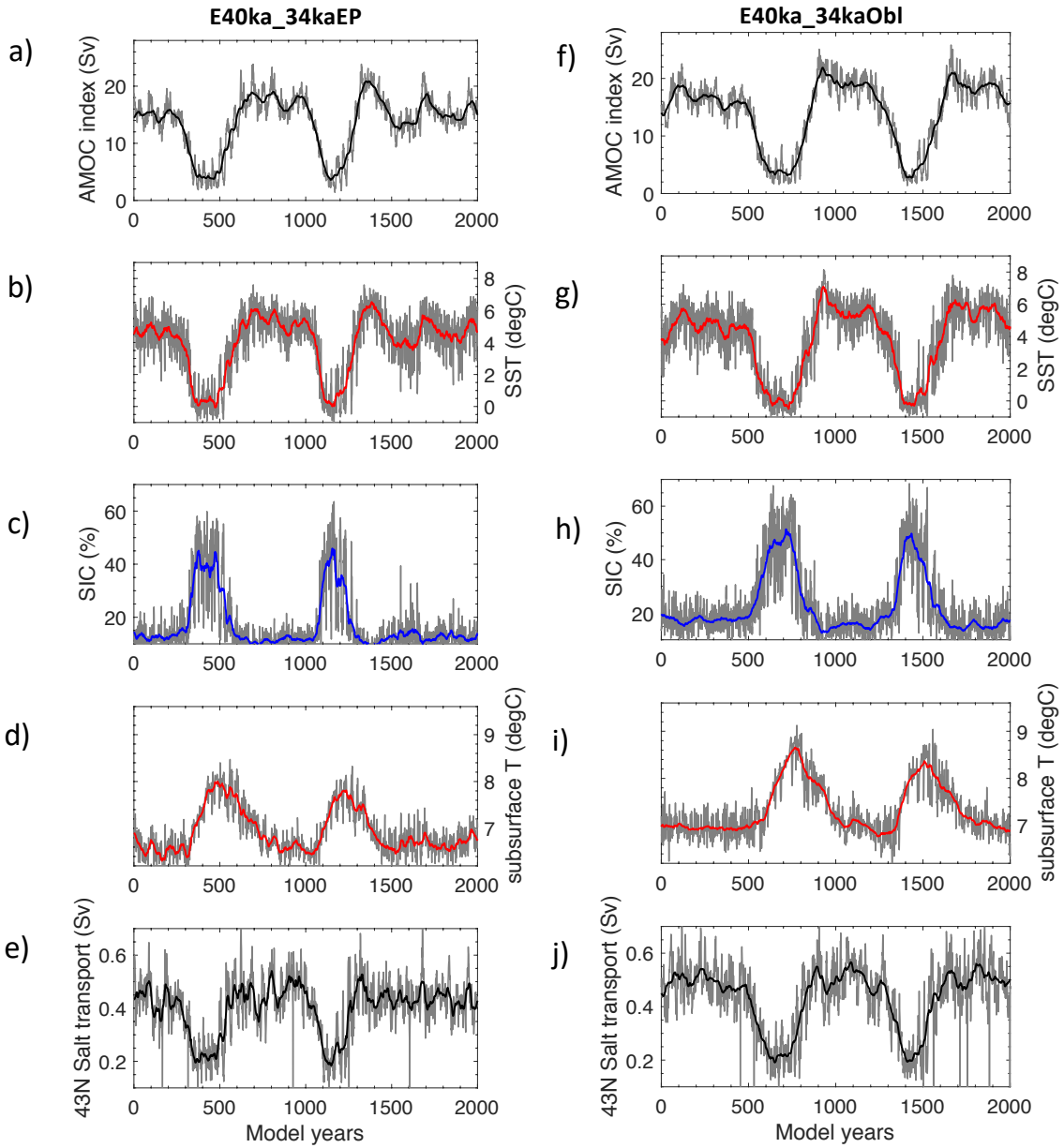
E40ka_34kaEP
E40ka_34kaObl
a)
b)
c)
d)
e)
f)
g)
h)
i)
j)
AMOC index (Sv)
SST (degC)
SIC (%)
subsurface T (degC)
43N Salt transport (Sv)
Model years
0
500
1000
1500
2000

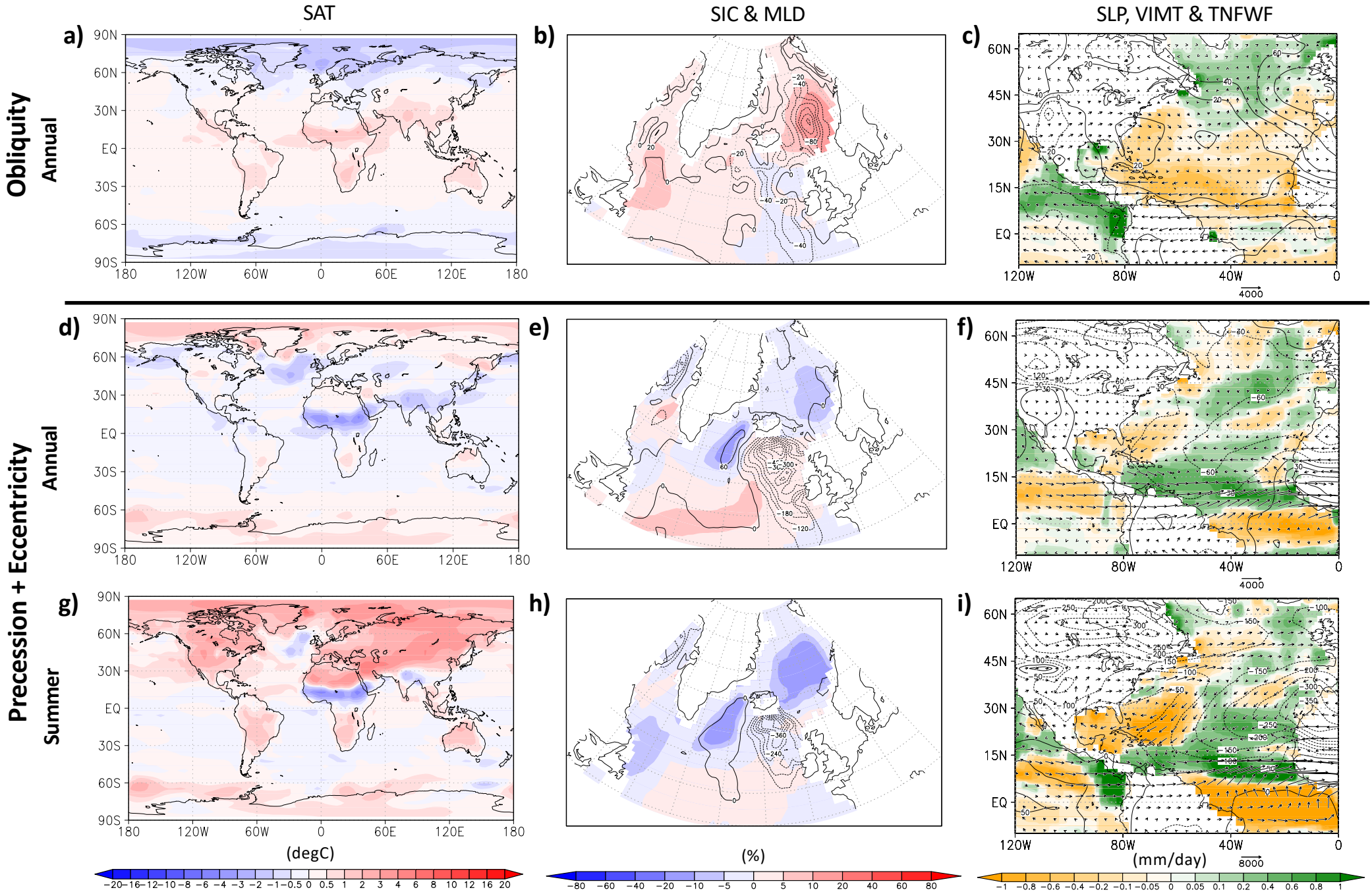
SAT
SIC & MLD
SLP, VIMT & TNFWF
Obliquity
Annual
Precession + Eccentricity
Annual
Summer
a)
b)
c)
d)
e)
f)
g)
h)
i)
90N
60N
30N
EQ
30S
60S
90S
180
120W
60W
0
60E
120E
180
60N
45N
30N
15N
EQ
120W
80W
40W
0
4000
8000
(degC)
(%)
(mm/day)
−20 −16 −12 −10 −8 −6 −4 −3 −2 −1 −0.5 0 0.5 1 2 3 4 6 8 10 12 16 20
−80 −60 −40 −20 −10 −5 0 5 10 20 40 60 80
−1 −0.8 −0.6 −0.4 −0.2 −0.1 −0.05 0 0.05 0.1 0.2 0.4 0.6 0.8 1

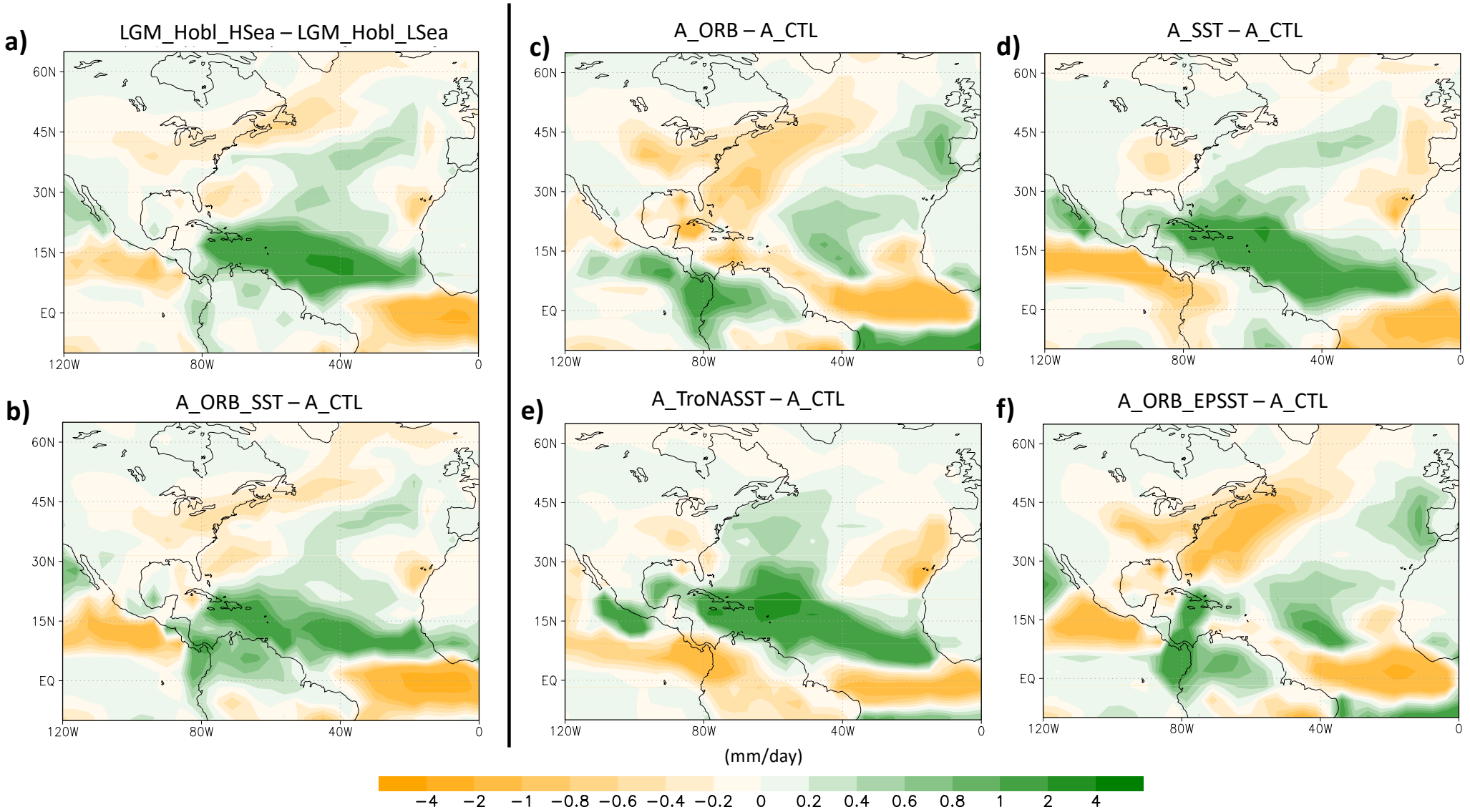
a)
LGM_Hobl_HSea – LGM_Hobl_LSea
b)
A_ORB_SST – A_CTL
c)
A_ORB – A_CTL
d)
A_SST – A_CTL
e)
A_TroNASST – A_CTL
f)
A_ORB_EPSST – A_CTL
60N
45N
30N
15N
EQ
120W
80W
40W
0
(mm/day)
−4 −2 −1 −0.8 −0.6 −0.4 −0.2 0 0.2 0.4 0.6 0.8 1 2 4

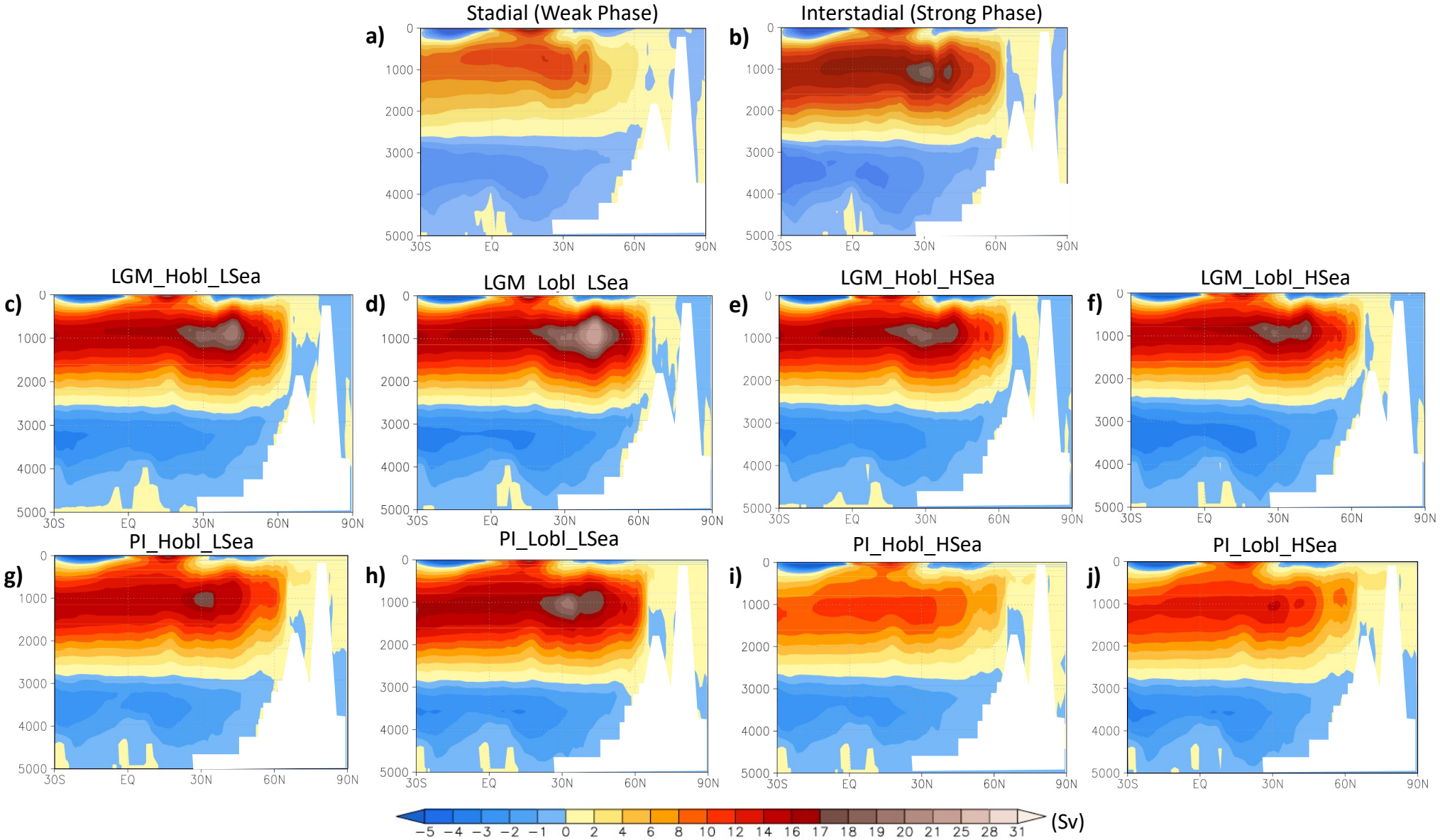
a)
Stadial (Weak Phase)
b)
Interstadial (Strong Phase)
c)
LGM_Hobl_LSea
d)
LGM_Lobl_LSea
e)
LGM_Hobl_HSea
f)
LGM_Lobl_HSea
g)
PI_Hobl_LSea
h)
PI_Lobl_LSea
i)
PI_Hobl_HSea
j)
PI_Lobl_HSea
0
1000
2000
3000
4000
5000
30S
EQ
30N
60N
90N
−5 −4 −3 −2 −1 0 2 4 6 8 10 12 14 16 17 18 19 20 21 25 28 31
(Sv)

COSMOS experiments

ID	Ecc.	Prec.	Obl.	Ice volume	Atm. CO_2	Initial ocean state	Integrated years
Control and hosing experiments							
E40ka_CTL	0.013	358°	23.6°	40ka	195	PI[54]	5000
E40ka_FWF	0.013	358°	23.6°	40ka	195	E40ka_CTL	2500
Transient experiment							
TRN40ka	40ka to 32ka BP			40ka	195	E40ka_CTL	250+5500
Equilibrium experiments under intermediate glacial conditions							
Role of constant orbital settings							
E40ka_34kaOrb	0.015	84.84°	22.6°	40ka	195	E40ka_CTL	5000
E40ka_34kaObl	0.013	358°	22.6°	40ka	195	E40ka_CTL	2000
E40ka_34kaEP	0.015	84.84°	23.6°	40ka	195	E40ka_CTL	2000
Role of internal climate backgrounds							
E40ka_34kaOrb_nCO2	0.015	84.84°	22.6°	40ka	185	E40ka_34kaOrb	5400
E40ka_34kaOrb_pCO2	0.015	84.84°	22.6°	40ka	205	E40ka_34kaOrb	5400
E40ka_34kaOrb_50kaICE	0.015	84.84°	22.6°	50ka	195	E40ka_34kaOrb	3200
E40ka_50kaICE	0.013	358°	23.6°	50ka	195	E40ka_34kaOrb_50kaICE	5400
E50ka	0.013	229.6°	24.4°	50ka	204	E40ka_50kaICE	5400
Sensitivity experiments under peak glacial and interglacial conditions							
LGM_HObl_HSea	0.04	90°	24.5°	LGM	185	LGM[54]	1500
LGM_HObl_LSea	0.04	270°	24.5°	LGM	185	LGM[54]	1500
LGM_LObl_HSea	0.04	90°	22°	LGM	185	LGM[54]	1500
LGM_LObl_LSea	0.04	270°	22°	LGM	185	LGM[54]	1500
PI_HObl_HSea	0.04	90°	24.5°	PI	280	PI[54]	1500
PI_HObl_LSea	0.04	270°	24.5°	PI	280	PI[54]	1500
PI_LObl_HSea	0.04	90°	22°	PI	280	PI[54]	1500
PI_LObl_LSea	0.04	270°	22°	PI	280	PI[54]	1500

AGCM sensitivity runs

ID	Ecc.	Prec.	Obl.	Sea surface conditions	Regional forcing	50
A_CTL	0.04	270°	24.5°	LGM_Hobl_LSea	\	50
A_ORB_SST	0.04	90°	24.5°	LGM_Hobl_HSea	\	50
A_ORB	0.04	90°	24.5°	LGM_Hobl_LSea	\	50
A_SST	0.04	270°	24.5°	LGM_Hobl_HSea	\	50
A_TroNASST	0.04	270°	24.5°	LGM_Hobl_LSea	Tropical North Atlantic SST is from *LGM_HObl_HSea*	50
A_ORB_EPSST	0.04	90°	24.5°	LGM_Hobl_LSea	Eastern Pacific SST is from *LGM_HObl_HSea*	50

Nr.	Core ID	Lat.	Lon.	Response during S-IS transition	Approximate Range (degC)	Simulated Value (degC)	Proxy	Ref.
	Northern Hemisphere							
1	GISP2 ice core	72.6	-38.5	warming	~8-16	2.57	ice core	Grootes et al. 1993; Huber et al. 2006[76,77]
2	ENAM93-21	62.73	-3.88	warming	~1-3	1.84	planktic foraminifer assemblages	Rasmussen et al. 1996; Rasmussen and Thomsen 2008[78,79]
3	LINK 17	~61.3	-3	warming	~2-5	3.21	planktic foraminifer assemblages	Rasmussen and Thomsen 2008[78]
4	ENAM 33	61.26	-11.12	warming	~2-4	5.60	planktic foraminifer assemblages	Rasmussen et al. 2002; Rasmussen and Thomsen 2008[78,80]
5	DAPC-02	58.97	-9.62	warming	~3-5	5.61	planktic foraminifer assemblages	Rasmussen et al., 2002; Rasmussen and Thomsen 2008[78,81]
6	ODP 980	55.43	-14.7	warming	~4-6	4.88	planktic $\delta^{18}O$	McManus et al 1999[4]
7	M23414	53.537	-20.29	warming	~3-5	3.85	planktic foraminifer diversities	Kandiano et al. 2004[82]
8	ODP 883	51.2	167.77	cooling	~2.5-4	-0.14	planktic foraminifer assemblages	Kiefer et al. 2001[83]
9	MD01-2412	44.53	145	warming	~2-6	1.05	alkenone	Harada et al. 2006[84]
10	MD01-2444	37.6	-10.13	warming	~2-5	3.23	alkenone	Martrat et al. 2007[85]
11	MD95-2043	36.15	-2.62	warming	~1-3	2.05	alkenone/pollen	Cacho et al. 1999[86]
12	ODP 893a	34.29	-120.37	warming	~3-5	0.09	planktic foraminifer assemblages	Hendy and Kennett 2000[87]
13	MD95-2036	33.69	-57.57	warming	~2-5	0.57	alkenone	Sachs and Lehmen 1999[88]
	Southern Hemisphere							
14	CD154 17-17k	-33.32	29.47	cooling	~2	0.12	planktic foraminifer Mg/Ca	Simon et al., 2013[89]
15	ODP Site 1233	-41	-74.45	cooling	~2-3	-0.28	alkenone	Lamy et al 2004[90]
16	MD97-2120	-45.53	174.93	cooling	~2-3	-0.01	planktic foraminifer Mg/Ca	Pahnke et al 2003[91]
17	MD07-3128	-52.66	-75.57	cooling	~1-2	-0.30	alkenone	Caniupan et al 2011[92]
18	EDML ice core	-75	0	cooling	~0.5-3	-0.14	ice core	EPICA member 2006[70]
19	Dome C ice core	-75.06	123	cooling	~1-3	-0.14	ice core	EPICA member 2004[93]
20	Byrd ice core	-80	-129	cooling	~1-3	-0.14	ice core	Blunier and Brook, 2001[94]

Nr.	Core ID	Lat.	Lon.	Response during S-IS transition	Simulated Values (mm/mon)	Proxy	Ref.
	Northern Hemisphere						
21	MD01-2348	~44	~5	humid	3.9	Pollen	Van Meerbeeck et al. 2011[74]
22	Tenaghi Philippon core	40.97	24.22	humid	3.1	Terrestrial archive	Mueller et al. 2011[95]
23	Hulu Cave	32.5	119.17	humid	3.6	Stalagmite δ^{18}O	Wang et al., 2001[96]
24	Peqiin Cave	32.58	35.19	humid	0.7	Cave speleothem δ^{18}O	Bar-Matthews et al., 2003[97]
25	Soreq Cave	31.45	35.03	humid	0.6	Cave speleothem δ^{18}O	Bar-Matthews et al., 2003[97]
26	Lake Tulane NAD27	27.59	-81.5	arid	0.6	Pollen and plant macrofossils	Grimm et al. 2006[73]
27	Dongge Cave	25.28	108.08	humid	1.7	Stalagmite δ^{18}O	Yuan et al., 2004[98]
28	SO90-111KL/SO90-136KL	23.1	66.48	humid	0.9	Total organic carbon	Schulz et al. 1998[99]
29	RC27-23/RC27-14	18	57.65	humid	0.8	δ^{15}N	Altabet et al. 2002[100]
30	Lake Peten Itza	16.92	-89.83	humid	1.2	Clay-gypsum	Hodell et al. 2008[101]
31	Socatra Island	12.5	54	humid	-1.2	Stalagmite δ^{18}O	Burns et al. 2003[102]
32	ODP hole 1002C	10.71	-65.17	humid	-4.4	Ti/Fe ratio	Peterson et al. 2000[103]
	Southern Hemisphere						
33	GeoB3104-1/GeoB3912-1	-3.67	-37.72	arid	4.1	Fe/Ca ratio	Jennerjahn et al. 2004[102]
34	Lake Tanganyika	-6.7	29.83	humid	1.3	leaf wax δD	Tierney, J. E. et al. 2008[104]
35	Lake Malawi MAL05-2A	-10.02	34.19	arid	-0.4	lake sediment	Brown et al., 2007[105]
36	Northeastern Brazilian calcite speleothems	-10.17	-40.83	arid	-1.7	Speleothem and travertine deposit	Wang et al. 2004[106]
37	Pacupahuain Cave Stalagmite P09-PH2	-11.24	-75.82	arid	-1.1	Speleothem calcite δ^{18}O	Kanner et al. 2012[107]
38	Lynch's crater	-17.62	146.17	arid	0.9	Degree of peat humification and ratio of sedges to grass	Turney et al. 2004[108]
39	Salar de Uyuni core	-20.23	-67.5	arid	-0.4	Natural r-rays	Baker et al. 2001[109]
40	Santana Cave Stalagmite St8	-24.53	-48.73	arid	2.4	Speleothem calcite δ^{18}O	Cruz et al. 2006[110]
41	Caverna Botuvera Stalegmites	-27.22	-49.15	arid	0.1	Speleothem calcite δ^{18}O	Wang et al., 2006[111]
42	Botuvera Cave Stalagmite Bt2	-27.22	-49.16	arid	0.1	Stalagmite δ^{18}O	Cruz et al. 2005[112]
43	CD 154-17-17k	-33.27	29.12	arid	3.1	Fe/K ratio	Ziegler et al., 2013[113]